DIPLOMARBEIT

Self-assembly of ionic liquid crystals into smectic phases

zur Erlangung des akademischen Grades

Diplom-Ingenieur

im Rahmen des Studiums

Technische Physik

eingereicht von

Ralf Wanzenböck
Matrikelnummer 00002527

ausgeführt am Institut für Theoretische Physik
der Fakultät für Technische Physik der Technischen Universität Wien

Betreuung
Betreuer: O.Univ.-Prof. Dipl.-Ing. Dr.techn. Gerhard Kahl
Mitwirkung: Dipl.-Ing. Benedikt Hartl

Wien, 17. Dezember 2019

Unterschrift Verfasser

Unterschrift Betreuer

Abstract

In soft matter theory the investigation and the prediction of ordered phases and the identification of their regions of stability are of paramount relevance. This holds also for ionic liquid crystals (ILCs) which have gained rapidly increasing interest, both from the applied as well as from the academic point of view. As indicated by their names, such systems combine properties and characteristic features of both liquid crystals as well as of ionic liquids.

The combination of their characteristic features, i. e. shape anisotropy as well as charges, make theoretical investigations extremely complicated; in this work these features are mimicked via a Gay-Berne potential and (screened) Coulombic interactions. In this thesis we have developed a numerical tool which is expected to identify the ordered ground state configurations of such systems in an efficient and - at the same time - highly reliable manner. This new algorithm optimizes the total energy of the system and is based on ideas of evolutionary algorithms which allows us to find minima in the energy surface even in high dimensional search spaces and for rugged energy landscapes.

As compared to spherical particles, we found that this algorithm requires substantial amendments, in order to properly take into account the asphericity of the particles (in particular for aspect ratios larger than two). Focusing on regions in parameter space which correspond to realistic ILC systems we have introduced suitable modifications of the original optimization algorithm; first runs indicate that the self-assembly scenario of ILCs is expected to be very rich, as the system parameters are varied. A few examples are highlighted in the thesis and discussed.

Kurzfassung

In der Theorie der weichen Materie sind die Vorhersage von geordneten Phasen und die Identifizierung von stabilen Regionen von größter Bedeutung. Das gilt auch für ionische Flüssigkristalle, die immer größeres Interesse aus der Wissenschaft und auch hinsichtlich möglicher Anwendungsbereiche hervorrufen. Wie es der Name schon vermuten lässt, verbinden solche Systeme die charakteristischen Eigenschaften von Flüssigkristallen und ionischen Flüssigkeiten.

Die Kombination aus Formanisotropie und Ladungen verkompliziert die theoretische Untersuchung solcher Systeme sehr. In der vorliegenden Arbeit werden diese charakteristischen Eigenschaften durch ein Gay-Berne Potential und (abgeschirmte) Coulomb Wechselwirkungen angenähert. Zur Untersuchung von diesen Systemen aus ionischen Flüssigkristallen wurde ein numerisches Werkzeug entwickelt, das geordnete Grundzustandskonfigurationen auf effiziente und, gleichzeitig, zuverlässige Weise identifizieren soll. Dieser neue Algorithmus optimiert die Gesamtenergie des Systems und baut dabei auf das Konzept evolutionärer Algorithmen auf, um in hochdimensionalen Parameterräumen Minima der Energieoberfläche zu finden.

Im Vergleich zur Untersuchung sphärischer Teilchen waren umfassende Anpassungen des Algorithmus notwendig, um die Asphärizität der zu behandelnden Teilchen (insbesondere für Achsenverhältnisse größer als zwei) korrekt berücksichtigen zu können. Mit Fokus auf jene Regionen im Parameterraum, die realistischen Systemen aus ionischen Flüssigkristallen entsprechen, wurden sinnvolle Änderungen am bestehenden Optimisierungsalgorithmus vorgenommen. Erste Ergebnisse deuten darauf hin, dass die Selbstorganisation von ionischen Flüssigkristallen unter Variation von Systemparametern eine hohe Vielfalt aufweist. In der vorliegenden Arbeit werden einige Beispiele vorgestellt und diskutiert.

Contents

List of Figures 9

1. Introduction 11

2. Theoretical Concepts 13
    2.1. Liquid Crystals (LC) . . . 13
        2.1.1. Categories . . . 13
    2.2. Ionic Liquid Crystals (ILC) . . . 16
        2.2.1. Properties . . . 16
        2.2.2. Applications of ILCs . . . 16

3. Model 19
    3.1. Basic Concept . . . 19
    3.2. Interaction Potentials . . . 20
        3.2.1. Lennard-Jones potential . . . 20
        3.2.2. Gay-Berne potential . . . 21
        3.2.3. Yukawa potential . . . 22
    3.3. Total Pair Potential . . . 23
    3.4. Lattice . . . 26
    3.5. Parameter Space of the Model . . . 27
        3.5.1. Limitations . . . 27
        3.5.2. Impact of Parameters . . . 28

4. Numerical Methods 33
    4.1. Memetic Search Algorithm . . . 33
    4.2. Order parameters (OP) . . . 38
    4.3. Implementation . . . 40
        4.3.1. Memetic Algorithm Framework: Atuin . . . 40
        4.3.2. Energy Kernel: LAMMPS . . . 42

5. Results 43
    5.1. Results obtained from biased evolution (BE) . . . 44
        5.1.1. Bias individuals . . . 44
        5.1.2. Results . . . 46

5.2. Results obtained from free evolution (FE) 48
5.2.1. General results 49
5.2.2. Complementary calculations 58

6. Summary and Conclusion 63

A. Algorithm Keywords 65

Bibliography 67

List of Figures

2.1. Illustration of LC phases 14
2.2. Illustration of smectic A and smectic C phases 15
2.3. Cholesteric and columnar phases 15

3.1. Schematic view of Gay-Berne ellipsoid 19
3.2. Lennard-Jones potential 20
3.3. Gay-Berne potential and schematic view 22
3.4. Total pair potential and schematic view 24
3.5. Contour plot of pair interaction for different charges and positions . 25
3.6. Contour plot of pair interaction with and without LJ-potential . . . 26
3.7. Total pair potential for different charge values 29
3.8. Total pair potential for different charge positions 30
3.9. Total pair potential for different Gay-Berne well depths 31

4.1. Visual representation of a genome 34
4.2. Flowchart of memetic evolution 35
4.3. Visual representation of a crossover move 36
4.4. Flowchart depicting offspring generation 37
4.5. Comparison of offspring with and without ramp compression 42

5.1. Bias individuals for $N = 5$ particles in unit-cell 45
5.2. Bias individuals for $N = 10$ particles in unit-cell 45
5.3. Energy per particle for various BE individuals 46
5.4. Layer spacing for various BE individuals 47

5.5. Unit-cells of converged BE individuals 47
5.6. Periodic continuation of a converged BE individual 48
5.7. Energy per particle for different charges and positions 50
5.8. Energy per particle after cross-injection 50
5.9. Hexagonal order in smectic layer 51
5.10. Smectic layers and corresponding clusters of COMs 52
5.11. Columns and corresponding clusters of COMs 52
5.12. Hexagonal order in smectic layer within column 53
5.13. Clusters of COMs in smectic layers within columns 53
5.14. Layer spacing for different charges and positions 55
5.15. Layer spacing on the interval $1.0 \leq q \leq 2.0$ for $D = \pm 1.8\ R$ 55
5.16. Column spacing for different charges and positions 56
5.17. Distances within unit-cell of $\mathcal{G}^{0.9|3}_{F(5)}$ 57
5.18. Average nearest neighbor COM distances within a layer 57
5.19. Charge dependent layer spacing for different packing fractions . . . 59
5.20. Zigzag alignment of the particles for $\epsilon_R = 1$. 59
5.21. Energy per particle for $\epsilon_R = 1$ 60
5.22. Charge dependent column spacing for $\epsilon_R = 1$ 60
5.23. Comparison of results for different particle numbers without charges 61
5.24. Hexagonal alignment for seven particles in unit-cell 62
5.25. Comparison of U/N for five and ten particles in the unit-cell 62

1. Introduction

The investigation of the properties of ionic liquid crystals (ILCs), i. e. anisotropic, charged particles, has seen a rapidly growing interest in recent years, both in academia as well as in technical applications. In particular the self-assembly capacities of such systems - that combine well documented related properties of liquid crystals [1, 2] as well as those of ionic liquids - into ordered states has attracted much attention.

Due to the complex interplay of shape anisotropy and charges the theoretical investigation of the properties of ILCs has turned out to be extremely complicated. Especially the high complexity of parameter space (i. e. both model and system parameters) poses a huge numerical challenge. In this thesis we approximate the interactions of ILCs via a total pair potential that includes a Gay-Berne (GB) potential (which features the asphericity of the particles) and a screened Coulomb potential (which takes the charges into account). We develop a numerical tool to identify emerging ordered ground state structures at zero temperature by optimizing the total energy of the system, which operates numerically efficient and in a reliable manner. We achieve this by implementing and extending memetic search strategies that are based on the ideas of evolutionary algorithms and local optimization.

One goal of this thesis is to gain a better understanding of the self-assembly capacities of ILC systems within the presented model. To this end we test and record the impact of several model parameters on the self-assembly scenarios of these particles.

A further aim of this work is to try to reproduce a zero temperature representation of the so-called wide smectic phase reported by Bartsch et al. [3]. We adopt and combine two kinds of evolutionary search strategies: Biased evolution (i. e. well-defined particle configurations are introduced into the population to steer the evolutionary process) and free evolution (i. e. allowing rather wide ranges of the parameters without imposing too strong of a bias into the calculation). Thus, we are able to verify if specific traits prevail and also study the self-assembly of ILCs without external intervention.

2. Theoretical Concepts

2.1. Liquid Crystals (LC)

Matter phases with properties of liquid as well as crystalline states are called liquid crystals (LC) or mesomorphic phases. P. G. de Gennes defines LCs as systems of non-spherical molecules, which show liquid-like order in one or more spatial directions and a degree of anisotropy. Because of the non-spherical shape of the molecules, orientational order arises [1, 2].

2.1.1. Categories

LCs can be categorized via different criteria, e. g. shape, the interplay of positional and orientational order (see Table 2.1 and Fig. 2.1) or emerging phases. The aforementioned mesomorphic phases consist of either elongated (calamitic), e. g. rod-like, cuboid or ellipsoid, or disk-like (discotic) molecules and emerge in various phases between liquid (isotropic) and crystalline, that may show long-range orientational and/or positional order [2].

	positional	orientational
isotropic	✗	✗
nematic	✗	✓
smectic	✓	✓
crystalline	✓	✓

Tab. 2.1.: Classification of LC phases via positional and/or orientational order.

Nematic Phases

In the nematic (N) phase the molecules show orientational but no positional order. Therefore, a preferred direction can be observed within the system. This feature

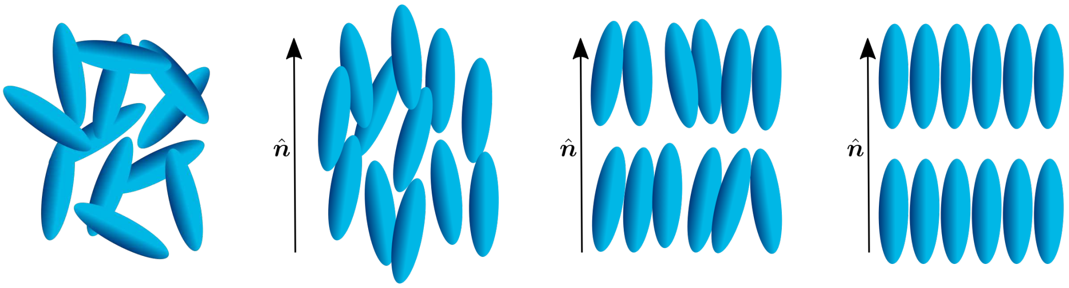

FIG. 2.1.: Overview of LC phases classified with respect to positional and orientational order. From left to right the figure shows isotropic, nematic, smectic A and crystalline phases.

can be quantified via the director $\hat{\boldsymbol{n}}$ which is the eigenvector corresponding to the largest eigenvalue of the symmetric and traceless tensor

$$Q_{ij} = \frac{1}{N} \sum_{\alpha=1} N \left(d_i^\alpha d_j^\alpha - \frac{1}{3} \delta_{ij} \right), \tag{2.1}$$

where N is the number of particles, the unit vector $\boldsymbol{d^\alpha}$ points along the long-axis of molecule α, and i and j denote the Cartesian coordinates x, y and z [1, 4].

For uniaxial molecules we can calculate the nematic order parameter S from the angle θ^α between molecule α and the preferred direction $\hat{\boldsymbol{n}}$ via

$$S = \frac{1}{2} \langle 3cos^2(\theta^\alpha - 1) \rangle = \frac{1}{2} \langle 3(\boldsymbol{d^\alpha} \cdot \hat{\boldsymbol{n}})^2 - 1 \rangle, \tag{2.2}$$

which can take on values between -0.5 and 1; $S = 1$ signifies perfect alignment of all molecules while $S = 0$ indicates isotropy. The special case $S = -0.5$ arises if all molecules are oriented perpendicular to the director $\hat{\boldsymbol{n}}$ [4].

Smectic Phases

Smectic (Sm) phases are characterized by orientational and positional order. Typically, the nematic order parameter S, defined in Eq. (2.1), of Sm phases is $S > 0.8$. The molecules are arranged in so called Sm layers where the molecule centers show one-dimensional translational correlation orthogonal to these layers. Different Sm phases can be distinguished depending on positional ordering within the layers and the angle ϕ^l between the layer normal $\hat{\boldsymbol{l}}$ and the director $\hat{\boldsymbol{n}}$. Smectic A (SmA) and Smectic C (SmC) show no positional order within the layers, while other Sm phases, e. g. Smectic B (SmB), do show positional order within the layers. In SmA and SmB ϕ^l is close to zero; however, SmC molecules are tilted with respect to $\hat{\boldsymbol{l}}$, see Fig. 2.2 [2].

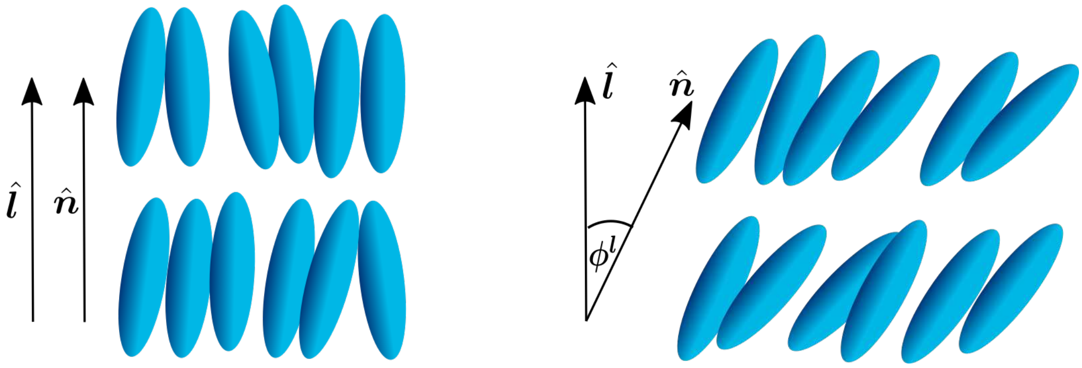

FIG. 2.2.: The left panel shows a 2D illustration of a smectic A phase, where the layer normal $\hat{\boldsymbol{l}}$ is parallel to the director $\hat{\boldsymbol{n}}$. On the right side the director $\hat{\boldsymbol{n}}$ is tilted by angle ϕ^l with respect to the layer normal $\hat{\boldsymbol{l}}$, constituting a smectic C phase.

Cholesteric Phases

Locally, cholesteric (Ch) phases show nematic order with no positional order, however, this preferred direction (director $\hat{\boldsymbol{n}}$) varies in space along the so-called cholesteric axis giving rise to a helical structure. Thus, Ch phases can be imagined as N phases that are twisted against each other [2]. See Fig. 2.3(a) to obtain a better picture of this phase.

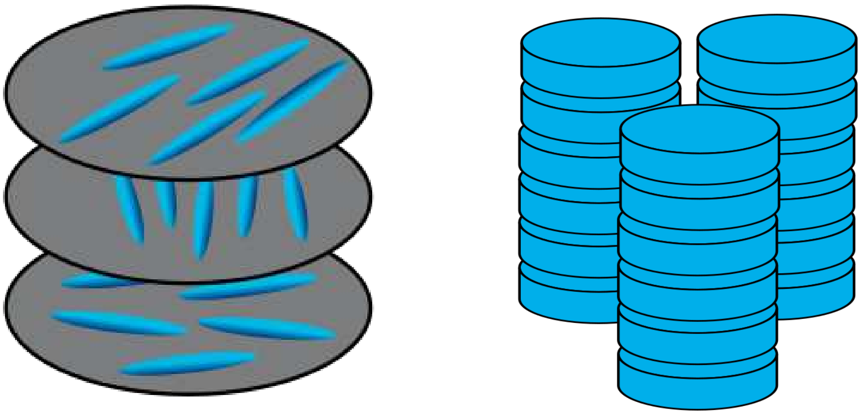

(a) cholesteric

(b) columnar

FIG. 2.3.: The left panel (a) shows a cholesteric phase, the right panel (b) presents a typical columnar phase of discotic molecules.

Columnar Phases

In columnar (C) phases we observe two-dimensional long-range positional order. C phases are usually depicted as stacks of discotic molecules similar to Fig. 2.3(b), although this shape is not a prerequisite for the emergence of columnar phases [1, 2].

2.2. Ionic Liquid Crystals (ILC)

Ionic liquid crystals (ILC) are LCs that carry charges and, therefore, combine properties of ionic liquids (ILs) and LCs [5].

2.2.1. Properties

ILCs are characterized by a very low vapor pressure and, for that reason, are suitable alternatives to more volatile organic solvents, such as electrolytes in solar cells. Due to the presence of charges, ILCs are susceptible to electric and magnetic fields, which has to be accounted for in the theoretical description (see chapter 3) and can be taken advantage of when controlling such effects. A further attractive feature of ILCs is the high ion conductivity that may arise in certain spatial dimensions, depending on mesophase. While the conductivity of columnar phases is restricted to one dimension (parallel to the columns), Sm phases exhibit high conductivity in two dimensions (namely perpendicular to the layer normal) [3, 5].

2.2.2. Applications of ILCs

The existing and envisioned applications of ILCs are manifold, including adaptive ion-conductive materials, dye-sensitized solar cells (DSSC), electrochromic materials and photoluminescent soft materials [6].

The following brief overview of these applications closely follows Ref. [6]:

- **Ion-conductive materials** consisting of ILCs could be used for molecular electronics or fuel cells, where the mobile ions carry the charges and, due to anisotropic properties, conductivity is direction dependent in one or two dimensions according to the mesophase of the material.
- Due to their superior conductivity ILCs might be an alternative to ionic liquids (IL) for replacing organic solvent electrolytes in **dye-sensitized solar cells (DSSC)**. Leakage and evaporation of these organic solvents reduce the lifetime of DSSCs, therefore, stable ILs or ILCs are promising alternatives.

- The color of **electrochromic materials** depends on an applied potential. Kato et al. introduce electrochromic properties of ILCs in Ref. [7].
- Because of the high mobility of the charge carrying ions, ILCs might be suitable candidates for **photoluminescent soft materials** such as organic light-emitting diodes (OLEDs).

3. Model

In this chapter we closely follow Refs. [3] and [8] in modeling Gay-Berne and Coulomb interactions for ILC molecules. Furthermore, Lennard-Jones spheres are utilized to guarantee repulsion at short distances.

3.1. Basic Concept

In principle, we treat ILC molecules as rigid prolate rotational ellipsoids that carry positive charges and interact through pair potentials consisting of Gay-Berne, Coulomb and Lennard-Jones interactions. The negative counter ions guaranteeing electric neutrality of the system are taken into account via a continuous background, thus screening the charges. Consequently, the Coulomb interactions between the different entities are replaced by a screened Coulomb potential, i. e. a Yukawa potential.

Each ILC molecule is modeled as an ellipsoid that may carry one or two point charges and is filled by non-overlapping spheres guaranteeing the steric repulsion of the molecules, see Fig. 3.1 for a simplified view.

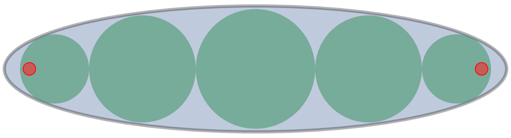

FIG. 3.1.: Cross-sectional schematic of a Gay-Berne ellipsoid with Lennard-Jones spheres (green) and carrying two point charges (red).

3.2. Interaction Potentials

3.2.1. Lennard-Jones potential

The Lennard-Jones (LJ) potential models the pairwise interaction of uncharged spherical particles via

$$U_{\mathrm{LJ}}(r) = 4\epsilon\left[\left(\frac{\sigma}{r}\right)^{12} - \left(\frac{\sigma}{r}\right)^{6}\right], \quad r < r_c, \tag{3.1}$$

with the well depth ϵ, a root σ and cutoff radius r_c, i. e. the maximum interaction range [9]. In this thesis we set $r_c = R_S$, where R_S is the sphere diameter, to approximate hard spheres and prevent overlaps. Fig. 3.2 shows a standard LJ potential (blue) and its truncated form with $r_c = R_S$ (red).

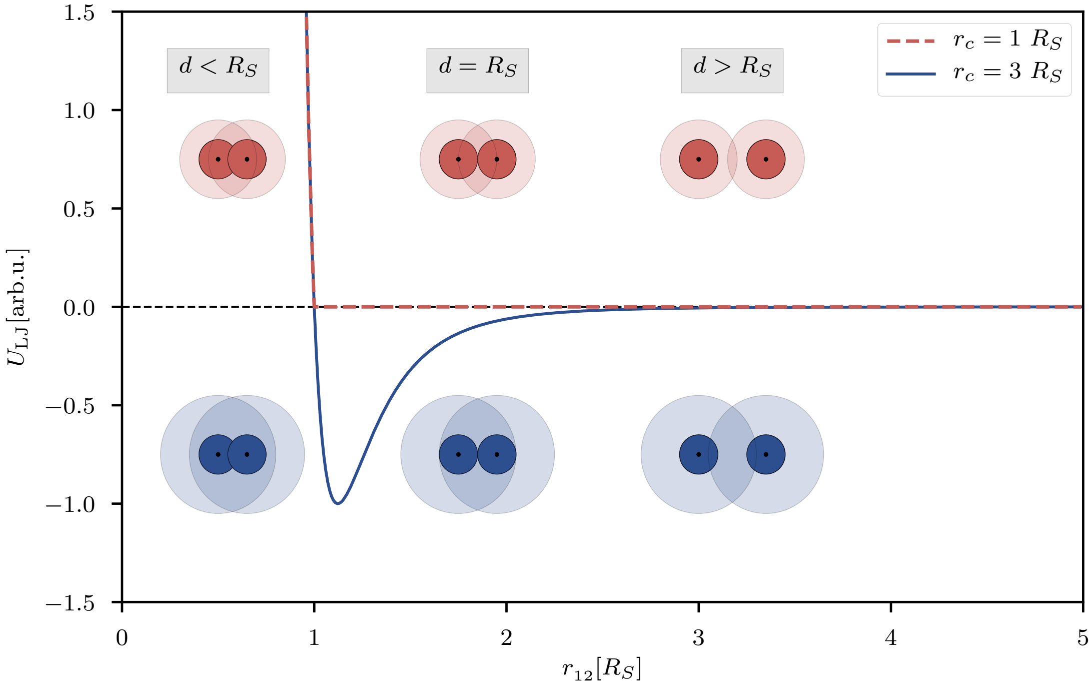

FIG. 3.2.: Comparison of a standard LJ potential (blue curve) versus a LJ potential where the cutoff radius r_c equals the sphere diameter R_S (red dashed curve), such that the spheres only interact if they overlap. The solid circles illustrate the relative position of the spheres, where R_S is the sphere diameter. The transparent spheres illustrate the cutoff r_c, i. e. the interaction range with respect to the sphere centers.

3.2.2. Gay-Berne potential

The Gay-Berne (GB) pair potential [10, 11] is a generalized LJ potential extended to non-spherical particles; it is a function of the vector $\boldsymbol{r_{12}}$ between the particle centers (centers of mass for non-symmetric, non-isotropic particles) and their respective spatial orientations $\boldsymbol{\omega_1}$ and $\boldsymbol{\omega_2}$ with respect to a fixed spatial axis [9, 12, 13]. By defining the interaction strength ϵ and the contact distance σ the GB potential can be expressed as

$$\begin{aligned} U_{\mathrm{GB}}(\boldsymbol{r_{12}}, \boldsymbol{\omega_1}, \boldsymbol{\omega_2}) = 4\epsilon(\boldsymbol{r_{12}}, \boldsymbol{\omega_1}, \boldsymbol{\omega_2}) \times \\ \Bigg[\left(1 + \frac{|\boldsymbol{r_{12}}|}{R} - \sigma(\boldsymbol{r_{12}}, \boldsymbol{\omega_1}, \boldsymbol{\omega_2}) \right)^{-12} \\ - \left(1 + \frac{|\boldsymbol{r_{12}}|}{R} - \sigma(\boldsymbol{r_{12}}, \boldsymbol{\omega_1}, \boldsymbol{\omega_2}) \right)^{-6} \Bigg], \end{aligned} \tag{3.2}$$

$$\begin{aligned} \epsilon(\boldsymbol{\hat{r}_{12}}, \boldsymbol{\omega_1}, \boldsymbol{\omega_2}) = \epsilon_0 \left(1 - (\chi \boldsymbol{\omega_1} \cdot \boldsymbol{\omega_2})^2\right)^{-\frac{\nu}{2}} \times \\ \Bigg[1 - \frac{\chi'}{2} \Bigg(\frac{(\boldsymbol{\hat{r}_{12}} \cdot \boldsymbol{\omega_1} + \boldsymbol{\hat{r}_{12}} \cdot \boldsymbol{\omega_2})^2}{1 + \chi' \boldsymbol{\omega_1} \cdot \boldsymbol{\omega_2}} \\ + \frac{(\boldsymbol{\hat{r}_{12}} \cdot \boldsymbol{\omega_1} - \boldsymbol{\hat{r}_{12}} \cdot \boldsymbol{\omega_2})^2}{1 - \chi' \boldsymbol{\omega_1} \cdot \boldsymbol{\omega_2}} \Bigg) \Bigg], \end{aligned} \tag{3.3}$$

$$\begin{aligned} \sigma(\boldsymbol{\hat{r}_{12}}, \boldsymbol{\omega_1}, \boldsymbol{\omega_2}) = \Bigg[1 - \frac{\chi}{2} \Bigg(\frac{(\boldsymbol{\hat{r}_{12}} \cdot \boldsymbol{\omega_1} + \boldsymbol{\hat{r}_{12}} \cdot \boldsymbol{\omega_2})^2}{1 + \chi \boldsymbol{\omega_1} \cdot \boldsymbol{\omega_2}} \\ + \frac{(\boldsymbol{\hat{r}_{12}} \cdot \boldsymbol{\omega_1} - \boldsymbol{\hat{r}_{12}} \cdot \boldsymbol{\omega_2})^2}{1 - \chi \boldsymbol{\omega_1} \cdot \boldsymbol{\omega_2}} \Bigg) \Bigg]^{-\frac{1}{2}}. \end{aligned} \tag{3.4}$$

Here ϵ_0 sets the energy scale of the pair interaction, the functions χ and χ' involve the well depths ϵ_R (side-by-side) and ϵ_L (end-to-end) and the diameters L (long axis) and R (short axis) of the ellipsoid. Fig. 3.3 shows a pair schematic and the GB potential for different relative orientations. The empirical exponents μ and ν are fixed as $\mu = 2$ and $\nu = 1$ according to [3]. These auxiliary functions are defined as

$$\chi(L, R) = \frac{(L/R)^2 - 1}{(L/R)^2 + 1}, \quad \chi'(\epsilon_R, \epsilon_L) = \frac{(\epsilon_R/\epsilon_L)^{\frac{1}{\mu}} - 1}{(\epsilon_R/\epsilon_L)^{\frac{1}{\mu}} + 1}. \tag{3.5}$$

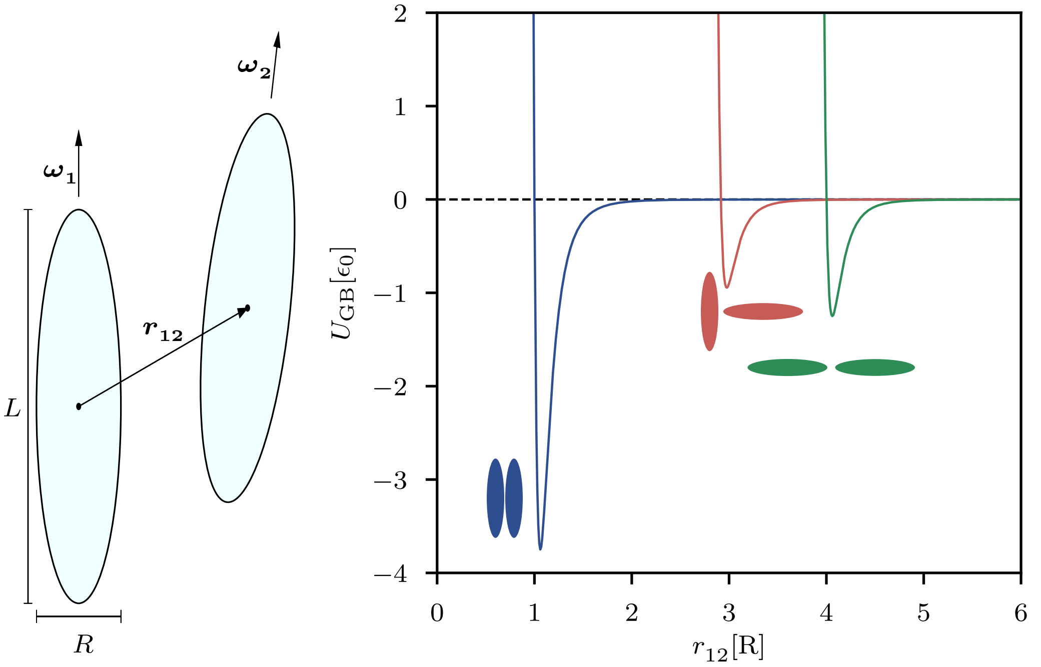

FIG. 3.3.: The left panel shows two rigid ellipsoids representing ILC molecules with center-to-center vector $\boldsymbol{r}_{12}$ and orientations $\boldsymbol{\omega}_1$ and $\boldsymbol{\omega}_2$. The right panel displays the resulting pair potential for three typical configurations of the molecules with parameters $L/R = 4$, $\epsilon_R/\epsilon_L = 3$ and $\mu/\nu = 2$ (see text).

3.2.3. Yukawa potential

When investigating ILCs the Coulomb interaction between charges has to be considered. The much smaller counterions are modeled as a continuous background, thus screening the charges of the ILCs. Placing charges q along the long axis of each ellipsoid in opposite directions at a distance D from the center, the Yukawa interaction between these charges reads

$$\begin{aligned} U_{\mathrm{Y}}(\boldsymbol{r}_{12}, \boldsymbol{\omega}_1, \boldsymbol{\omega}_2) = \gamma \Bigg[&\frac{\exp\left(-\frac{|\boldsymbol{r}_{12}+D(\boldsymbol{\omega}_1+\boldsymbol{\omega}_2)|}{\lambda_{\mathrm{db}}}\right)}{|\boldsymbol{r}_{12} + D(\boldsymbol{\omega}_1 + \boldsymbol{\omega}_2)|} + \frac{\exp\left(-\frac{|\boldsymbol{r}_{12}+D(\boldsymbol{\omega}_1-\boldsymbol{\omega}_2)|}{\lambda_{\mathrm{db}}}\right)}{|\boldsymbol{r}_{12} + D(\boldsymbol{\omega}_1 - \boldsymbol{\omega}_2)|} \\ &+ \frac{\exp\left(-\frac{|\boldsymbol{r}_{12}-D(\boldsymbol{\omega}_1+\boldsymbol{\omega}_2)|}{\lambda_{\mathrm{db}}}\right)}{|\boldsymbol{r}_{12} - D(\boldsymbol{\omega}_1 + \boldsymbol{\omega}_2)|} + \frac{\exp\left(-\frac{|\boldsymbol{r}_{12}-D(\boldsymbol{\omega}_1-\boldsymbol{\omega}_2)|}{\lambda_{\mathrm{db}}}\right)}{|\boldsymbol{r}_{12} - D(\boldsymbol{\omega}_1 - \boldsymbol{\omega}_2)|} \Bigg], \end{aligned} \tag{3.6}$$

with the electrostatic energy scale $\gamma{=}q^2/(4\pi\varepsilon)$, permittivity ε and the Debye screening length

$$\lambda_{\mathrm{db}} = \sqrt{\frac{kT}{q^2\rho_c}}. \tag{3.7}$$

With respect to γ we define the unit charge $q_0 = \sqrt{4\pi\varepsilon\gamma}$; all charge values in this work are given in units of q_0 if not explicitly stated otherwise. As we are investigating possible ground states at temperature $T = 0\ K$, λ_{db} can not be solely calculated from system parameters. We follow [3] and define $\lambda_{\mathrm{db}}^{(q=1)} = 5$. The screening lengths for different charge values are calculated by applying the factor $1/q$. Furthermore, we introduce the total charge of one ellipsoid as $Q = 2q$.

Within this thesis all charges q are positive and result in a purely repulsive interaction. The interactions between charges within the same ellipsoid are not taken into account, the ellipsoids are rigid.

3.3. Total Pair Potential

The sum of the Gay-Berne, the Yukawa and the Lennard-Jones potentials leads to the total pair potential

$$U(\boldsymbol{r_{12}}, \boldsymbol{\omega_1}, \boldsymbol{\omega_2}) = U_{\mathrm{GB}}(\boldsymbol{r_{12}}, \boldsymbol{\omega_1}, \boldsymbol{\omega_2}) + U_{\mathrm{Y}}(\boldsymbol{r_{12}}, \boldsymbol{\omega_1}, \boldsymbol{\omega_2}) + U_{\mathrm{LJ}}(\boldsymbol{r_{12}}, \boldsymbol{\omega_1}, \boldsymbol{\omega_2}), \tag{3.8}$$

as shown in Fig. 3.4.

Fig. 3.5 shows in contour plots a comparison of the total pair potential as the charges q and their positions vary. Their effect is clearly noticeable beyond the range of the short-range GB interaction.

Fig. 3.6 shows the effect of the relative orientation of the ellipsoids on the total pair potential. The blue ellipsoid is fixed, the orientation of the green ellipsoid is varied in space. Without the LJ-interaction low-energy areas appear in the middle of the contour plots for significant overlaps (shown in row one), thus motivating the inscription of LJ-spheres to suppress such configurations. The addition of LJ-spheres with $r_c = R_S$ (cutoff radius r_c, sphere radius R_S) within the ellipsoids leads to the interaction energies shown in row two and guarantees that all overlaps are energetically unfavorable.

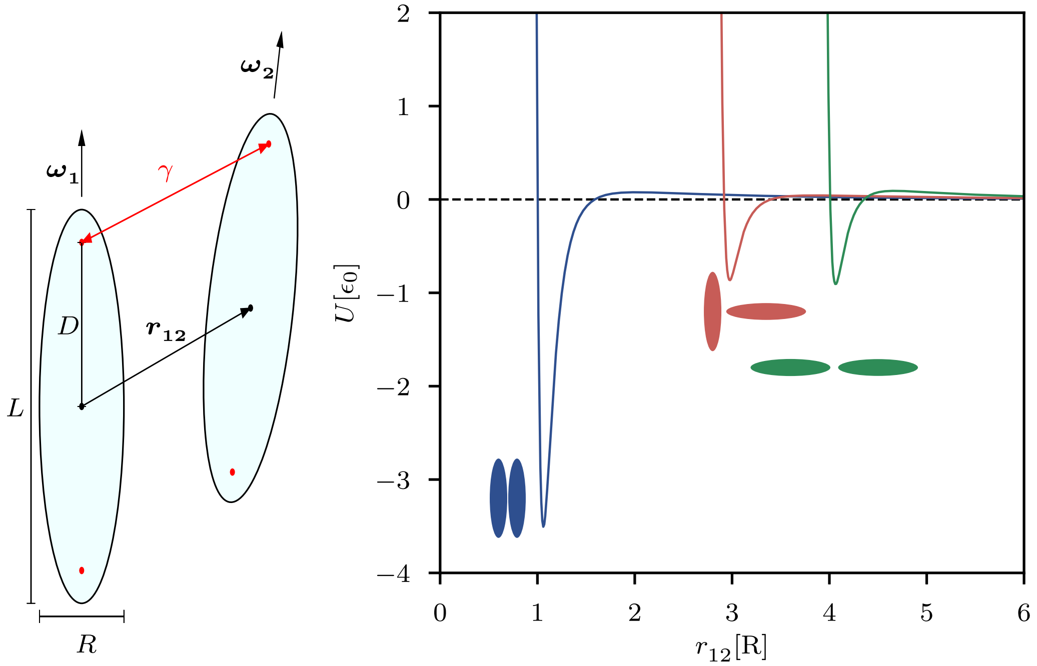

FIG. 3.4.: The left panel shows two rigid ellipsoids representing ILC molecules with center-to-center distance $\boldsymbol{r_{12}}$, orientations $\boldsymbol{\omega_1}$, $\boldsymbol{\omega_2}$ and charges on the long axis. The right panel displays the resulting total pair potential (see Eq. (3.8)) for this configuration with parameters $L/R = 4$, $D = \pm 1.8\ R$, $\epsilon_R/\epsilon_L = 3$, $\mu/\nu = 2$, $\gamma/(R\varepsilon_0) = 0.045$, $q = 2$ and $\lambda_{\text{db}}^{(q=2)} = 2.5\ R$.

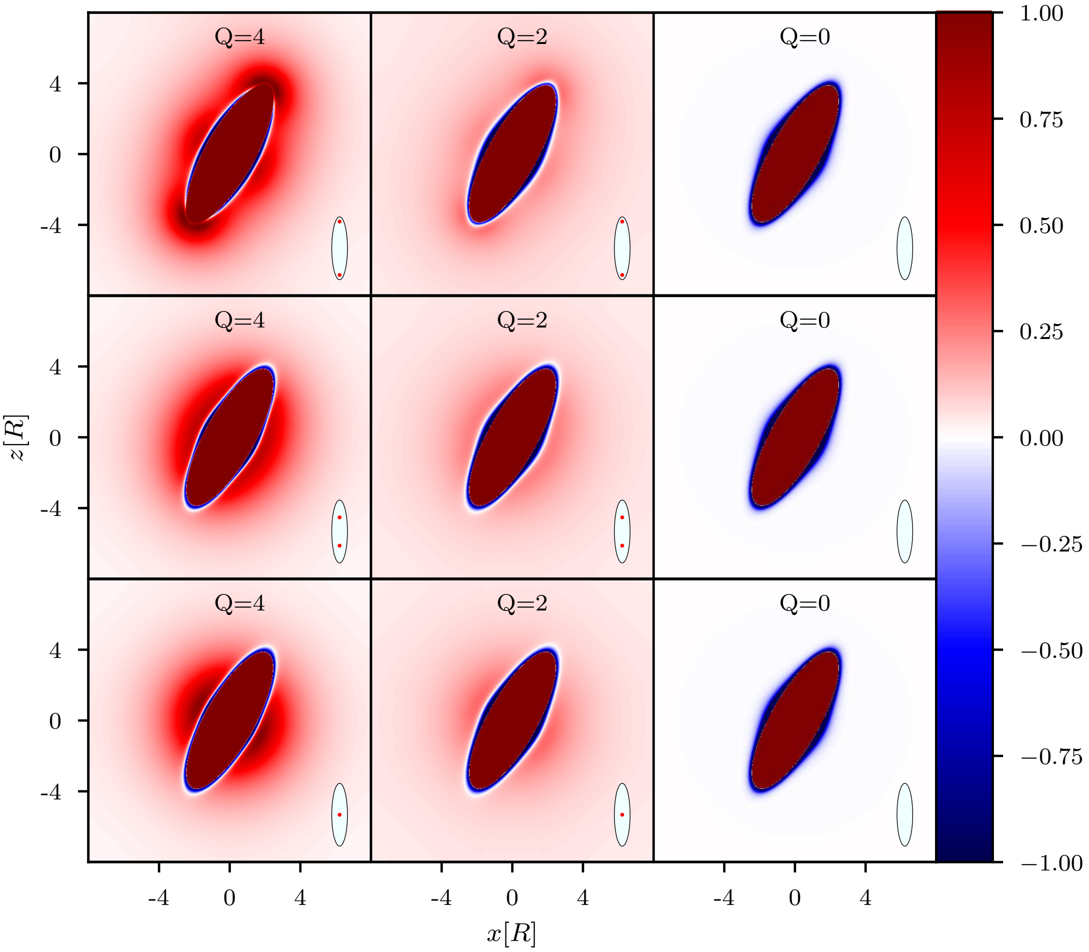

FIG. 3.5.: Comparison of the total pair potential of two ellipsoids in a contour plot, depending on the total charge Q and the position of the charges. In row one the charges are located at the tips of the ellipsoids ($D = \pm 1.8\ R$), while in the second row they are midway from the center ($D = \pm 0.9\ R$) and in row three one charge is placed at the ellipsoid center. In the case of two charges each carries $Q/2$. One ellipsoid is fixed at the center and the position of the other ellipsoid varies on the x-z-plane. The angle between the long-axes of the ellipsoids is $\pi/8$. The energies exceed $U = 1$ by orders of magnitude, but are truncated in this figure to outline the behavior at the ellipsoid margins and the effect of the charges.
Parameters: $\epsilon_R/\epsilon_L = 3$, $L/R = 4$, $\gamma/(R\varepsilon_0) = 0.25$, $\lambda_{\text{db}}^{(Q=2)} = 2.5\ R$ and $\lambda_{\text{db}}^{(Q=4)} = 1.25\ R$.

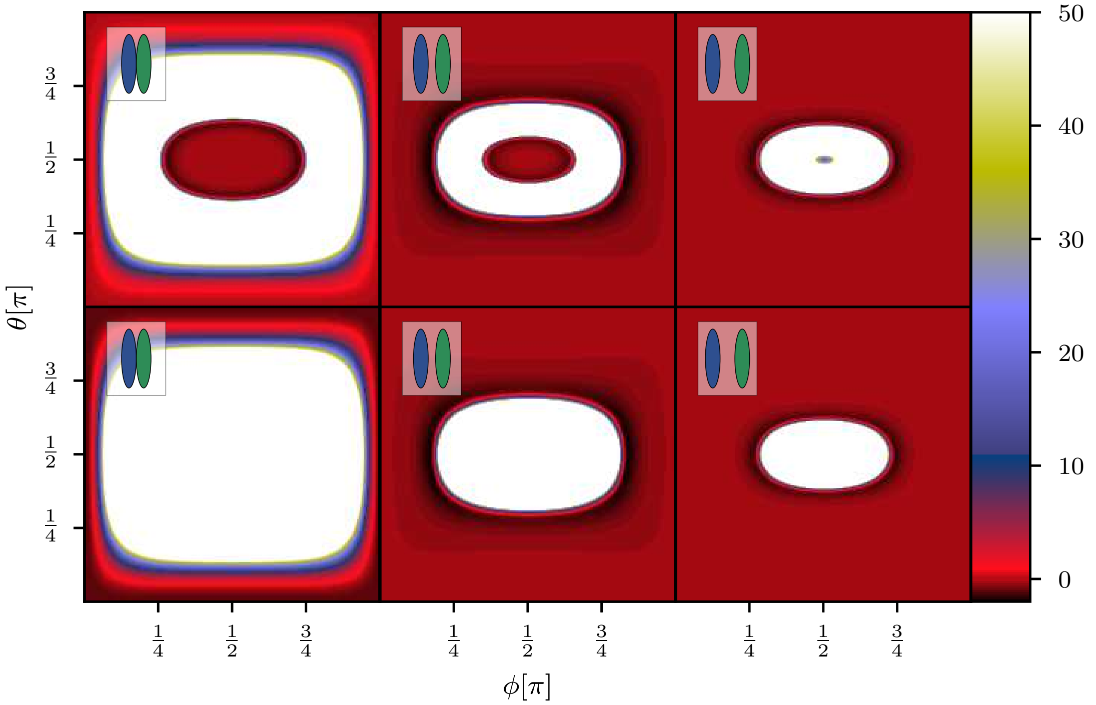

FIG. 3.6.: Comparison of the total pair potential between two ellipsoids without LJ-spheres with respect to the center-to-center distance r_{12} (1 R, 1.5 R and 2 R from left to right) and their relative orientation. The first row shows contour plots for the pair potential without LJ spheres, the contour plots in the second row show the total pair potential. The orientation of the blue ellipsoid is fixed while the green ellipsoid rotates along the spatial angles ϕ and θ. The energies go orders of magnitude beyond 50, but are truncated in this figure to outline the behaviour at the ellipsoid margins. Parameters: $\epsilon_R/\epsilon_L = 3$, $L/R = 4$, $\gamma/(R\varepsilon_0) = 0.25$, $q = 2$ and $\lambda_{\text{db}}^{(q=2)} = 2.5\ R$. Two charges are positioned at the ellipsoid tips at a distance $D = \pm 1.8\ R$ from the center.

3.4. Lattice

We define a three-dimensional unit-cell $\mathbb{V} = (\boldsymbol{a}, \boldsymbol{b}, \boldsymbol{c})$ with $\boldsymbol{a} = (a_x, a_y, a_z)$, $\boldsymbol{b} = (0, b_y, b_z)$, $\boldsymbol{c} = (0, 0, c_z)$ and the volume $V = a_x b_y c_z$. The vector elements a_y, a_z, and b_z encode the relative tilts of the base vectors with respect to the Cartesian axes. Periodic continuation in all three spatial dimensions gives rise to the lattice

$$\mathcal{G} = \mathcal{G}(\boldsymbol{R}^N, \boldsymbol{P}^N, \mathbb{V}) = \{\boldsymbol{R}^N, \boldsymbol{P}^N, \mathbb{V}\}, \tag{3.9}$$

with number of molecules N in the unit-cell, center-of-mass (COM) position $\boldsymbol{R}$ and orientation $\boldsymbol{P}$ of each molecule.

3.5. Parameter Space of the Model

Table 3.1 contains a comprehensive, but not exhaustive, list of parameters that can be varied. The dimension of the parameter space of the model is rather large. Thus the full range of parameters cannot be fully investigated within this thesis.

Parameter	**Description**
N	Number of particles in the unit-cell.
η_0	Packing fraction, i. e. volume V_e occupied by ellipsoids divided by the total available volume. $V_e = (4/3)\pi LRR$.
D	Distance along long-axis between ellipsoid center and charges.
R	Ellipsoid width along short-axis.
L/R	Ellipsoid length-to-width ratio, i. e. aspect ratio κ.
ϵ_R	Side-by-side GB potential well depth.
ϵ_L	End-to-end GB potential well depth.
μ, ν	Empirical exponents related to $\epsilon(\hat{\boldsymbol{r}}_{\mathbf{12}}, \boldsymbol{\omega}_{\mathbf{1}}, \boldsymbol{\omega}_{\mathbf{2}})$ (Eq. (3.3), Eq. (3.5)).
N_q	Number of point charges per ellipsoid.
q_i	Strength of the point charges.
λ_{db}	Debye screening length (screening due to counterions).
$\{\boldsymbol{a}, \boldsymbol{b}, \boldsymbol{c}\}$	Default base vectors (lengths, tilts and bounds) as a starting bias for the optimization.

Tab. 3.1.: Parameters that characterize the system under investigation.

3.5.1. Limitations

A scan over the total parameter space would quickly pass beyond any computational possibilities. Alternatively, an investigation on a wide mesh of parameters is not a promising strategy either ("stabs in the dark"). For these reasons, it is more appropriate to fix a few parameters, inspired by the configurations and related results presented in Ref. [3] or gathered from preliminary calculations of smaller systems. Table 3.2 shows the fixed parameter values.

Parameter	**Value**
Charge count N_q	2
Ellipsoid short axis R	1
Ellipsoid long axis L	4
Well depth end-to-end ϵ_L	1
Exponent μ	2
Exponent ν	1

TAB. 3.2.: Fixed values of model parameters to reduce the complexity of the parameter space.

3.5.2. Impact of Parameters

In an effort to better understand the impact of the different model parameters we investigate their influence on the system behavior. From these findings we then identify promising parameter combinations and/or ranges of values, for which we perform more focused parameter scans.

Default base vectors and bounds ($\mathbb{V} = (\boldsymbol{a}, \boldsymbol{b}, \boldsymbol{c})$)

The default unit-cell base and, more so, the associated bounds influence the available lattice configurations. If, for instance, strong tilts are suppressed, very flat unit-cells are not accessible for the algorithm introduced in chapter 4. On the other hand, strong tilts and extreme bounds (e. g. the possibility of very flat unit-cells), negatively affect the stability of the energy calculations in LAMMPS (see 4.3.2).

Number of particles (N)

The number of particles per unit-cell determines the dimension of the phase space and limits the possible configuration patterns. In principle, a higher particle number allows for more complex configurations but also severely impairs the calculation time (see chapter 5).

Charge related quantities (N_q, q_i, λ_{db}, D)

The different parameters related to the charges directly influence the total pair potential. To reduce the complexity of the parameter space we set $N_q = 2$ following [3] and, moreover, only use identical charges. The charge position denoted by distance D is varied from the ILC molecules tips to their center, where the two charges are

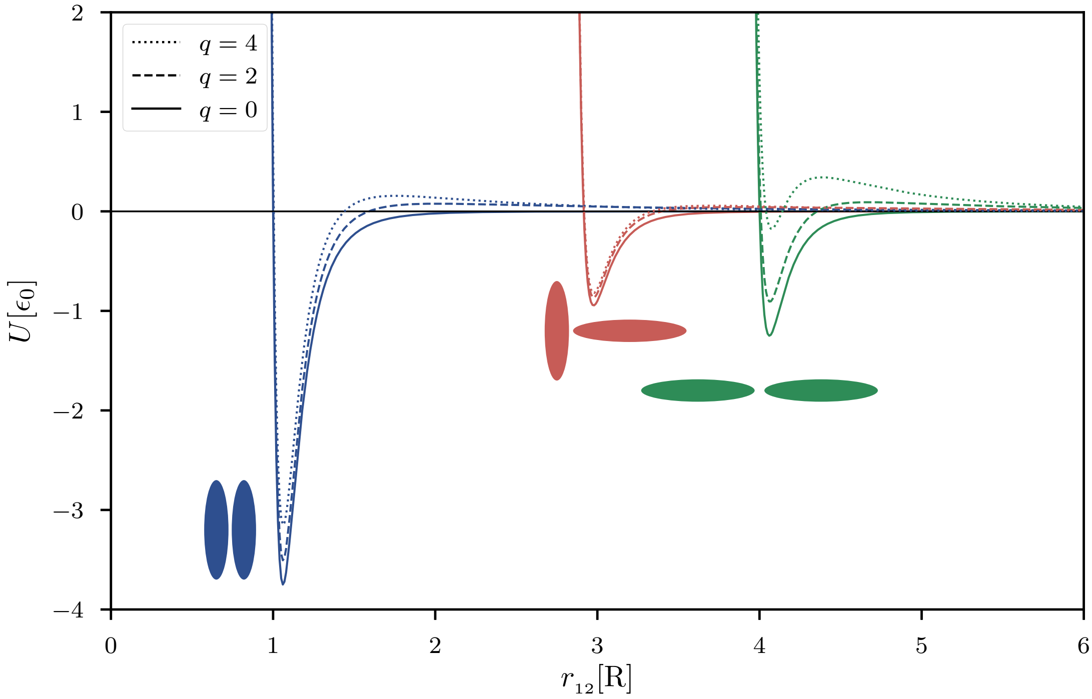

FIG. 3.7.: Comparison of the total pair potential for three archetypical ellipsoid configurations with respect to different charge strengths q. The charges are placed at $D = \pm 1.8\ R$.

replaced by one charge with $Q = 2q$. In parameter scans we investigate the influence of different charge strengths $q_i = q$ on the total pair potential.

In Fig. 3.7 we compare the total pair potential calculated for different values of q and corresponding screening lengths λ_{db} (see Eq. (3.7)) with all other parameters unchanged. While the side-by-side configuration remains the energy minimum, the 'T'-form takes precedence over an end-to-end formation for higher charges. Fig. 3.8 illustrates the effect of charge position D on the total pair potential; we notice that the 'T'-form is unaffected by the charge position.

Packing fraction (η_0)

The packing fraction η_0 is an important model parameter since it defines the available space within the unit-cell. With constant ellipsoid volume $V_e = (4/3)\pi LRR$ the unit-cell volume V is given by

$$V = \frac{NV_e}{\eta_0}. \tag{3.10}$$

Die approbierte gedruckte Originalversion dieser Diplomarbeit ist an der TU Wien Bibliothek verfügbar.
The approved original version of this thesis is available in print at TU Wien Bibliothek.
TU Bibliothek Your knowledge hub WIEN

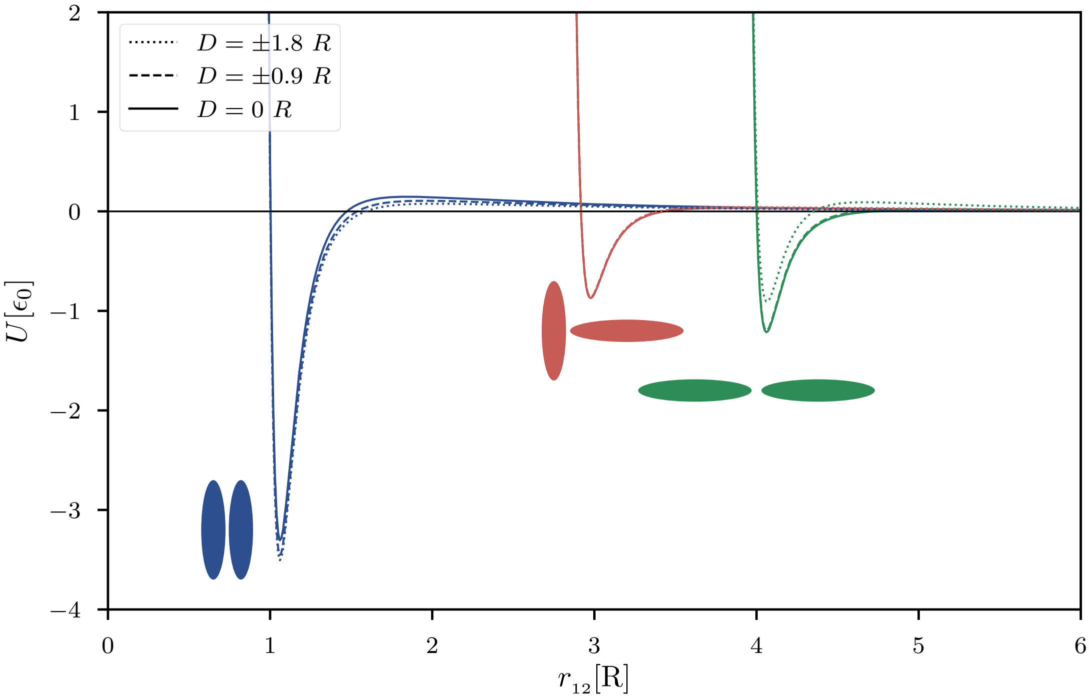

FIG. 3.8.: Comparison of the total pair potential for three charge positions. Two charges are placed at $D = \pm 1.8\ R$, $D = \pm 0.9\ R$ and $D = 0\ R$ respectively. At $D = 0\ R$ the two charges are replaced by one charge with $Q = 2q$.

Gay-Berne parameters (ϵ_R, ϵ_L, μ, ν)

The ratio between the side-by-side well depth ϵ_R and its end-to-end counterpart ϵ_L directly influences the GB pair potential. Following [3] we set $\epsilon_R/\epsilon_L = 3$ for the majority of calculations. For μ and ν we have chosen $\mu = 2$ and $\nu = 1$.

In Fig. 3.9 we compare the influence of ϵ_R/ϵ_L on the total pair potential (for simplicity $q = 0$).

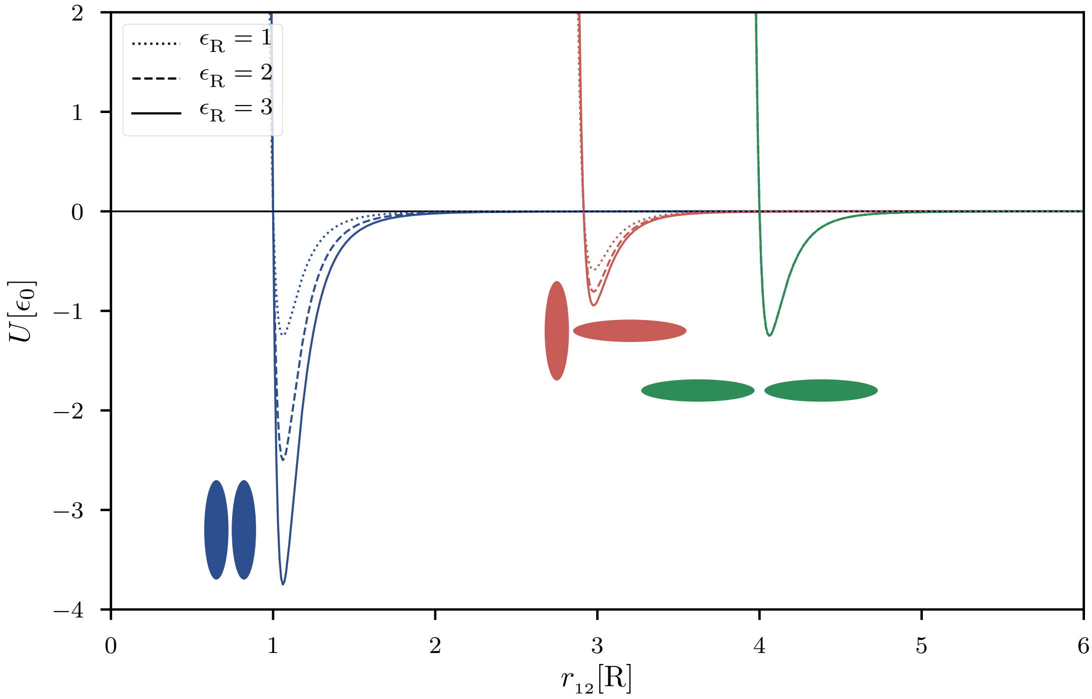

FIG. 3.9.: Comparison of the total pair potential for three archetypical ellipsoid configurations as ϵ_R is varied and setting $\epsilon_L = 1$. Noticeably, the end-to-end configuration is insensitive to ϵ_R/ϵ_L. The values of the charges have been set to zero.

4. Numerical Methods

In order to investigate the global minimum of the internal energy U, i. e. the sum over the pair interactions characterized in Eq. (3.8), and thus identify ordered ground states of the system described in chapter 3, we introduce a so-called memetic search algorithm (MA) [14]. MAs incorporate local steepest gradient descent optimization (LG) [15, 16] into evolutionary search strategies (EA) [14], i. e. mutation and selection mimicking the process of biological evolution. The inclusion of LG significantly improves the convergence rate of the algorithm. Subsequently, we define order parameters that allow us to quantify and to distinguish qualitatively different configurations in a computationally useful manner. Finally, we outline our computational implementation and limitations thereof [17].

Appendix A of the thesis contains definitions of the key terminology that is introduced in the following discussion.

4.1. Memetic Search Algorithm

An MA combines two strategies: evolutionary search and local optimization. In order to utilize EAs specific points in phase space are represented as unique genomes. With respect to Eq. (3.9) we define genomes via $\mathcal{G}_i = \{\boldsymbol{R}^N, \boldsymbol{P}^N, \mathbb{V}\}_i$, where i is one specific composition and each $\boldsymbol{P}_j$ $(j = 1, \ldots, N)$, is symmetrical when rotated by π. Thus, each genome contains the COM positions of all molecules $\boldsymbol{R}^N$ in the unit-cell, followed by all their respective orientations $\boldsymbol{P}^N$ and, lastly, the lattice vectors $\mathbb{V}$ which define the unit-cell (see Fig. 4.1). We refer to these genomes as ‘individuals’ or ‘lattice configurations’. The idea of EAs is based on biological evolution [18], such that genetic information of different individuals (‘parents’) is mixed in order to find a better solution to a given problem. When more suitable lattice configurations (‘offspring’) arise, others have to be removed from the gene pool. Even though the genome differentiates between positions and orientations, we restrict the algorithm to treat molecules as a whole when performing evolutionary crossover moves. Moreover, $\mathbb{V}$ is taken from one parent, i. e. the properties of the parents’ unit-cells are not mixed.

We closely follow Refs. [17, 19, 20] in detailing the MA. We utilize the same implementation as in Ref. [17].

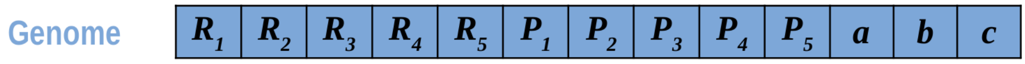

FIG. 4.1.: Visual representation of a genome $\mathcal{G}_i = \{\boldsymbol{R}^N, \boldsymbol{P}^N, \mathbb{V}\}_i$ for a unit-cell containing $N = 5$ molecules, with positions $\boldsymbol{R}_j$, orientations $\boldsymbol{P}_j$ and lattice base $\mathbb{V} = (\boldsymbol{a}, \boldsymbol{b}, \boldsymbol{c})$.

To employ EAs we first generate a pool of individuals, either with random or predefined properties, that constitute the initial population $\mathcal{G}^{N_p}$, where N_p is the number of individuals ('pool size'). While it is possible to increase or reduce the population size, N_p is typically kept constant. The individuals within the population are ordered according to their respective internal energy U. These high-quality individuals constitute the so-called elite and are protected against extinction. The pool is subject to continuous changes as more suitable or diverse offspring replace others. The rules and conditions regarding replacement are detailed below.

The following iterative steps regarding offspring creation and evaluation can be performed by multiple parallel processes, i. e. workers, and their results consolidated by a main process that manages population changes. Each iteration either produces a new lattice configuration or tries to improve an existing genome. These results are either inserted into the population or rejected and discarded. Every change in the pool composition constitutes a new generation; in this context 'generation' does not correspond to the familiar biological meaning [21]. The flowcharts in Fig. 4.2 and Fig. 4.4 depict the iterative process.

I. **Create offspring**
The creation of offspring takes place in parallel as every worker is instructed to generate new and/or improved lattice configurations. Each worker employs the procedure shown in Fig. 4.4.

   1. *Choose parents*
   One or more individuals are randomly selected from the population to become the parents of offspring $\mathcal{G}_{\text{off}}$. The choice may either be completely random or can be biased to favor the best individuals ('elite population' or 'elite') to a certain degree by performing 'roulette wheel'-selection, i. e. the selection probability is proportional to the fitness (see step II.2) [22]. The proportion of elite individuals within a population can be specified. With a certain given probability only one parent is chosen such that $\mathcal{G}_{\text{off}} = \mathcal{G}_i$; in that case the algorithm continuous with step I.3 'random mutation'.

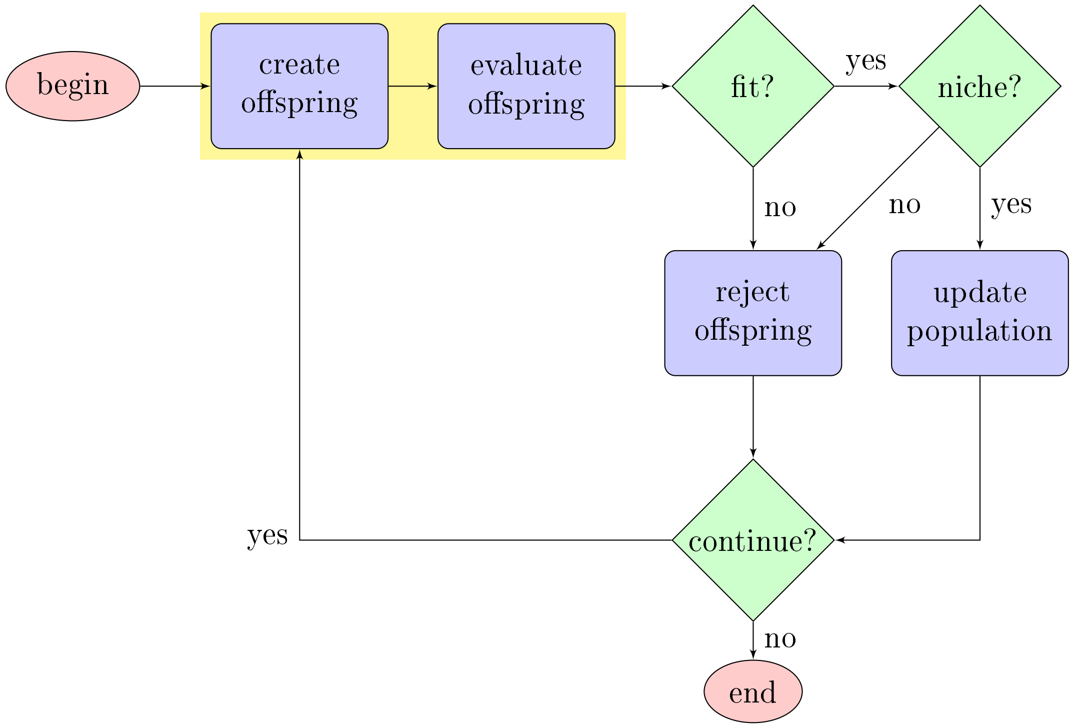

FIG. 4.2.: Flowchart showing one iteration step within the memetic evolution. The subprocesses 'create offspring' and 'evaluate offspring' (both highlighted in yellow) are carried out in parallel by all available workers, each producing offspring as shown in Fig. 4.4. Each new offspring is accepted or rejected depending on its fitness and available niches.

2. *Crossover*
   The parents are labeled as $\mathcal{G}_i$ and $\mathcal{G}_j$ according to Eq. (3.9) and their genomes are combined via a cut-and-splice variant of a crossover move as depicted in Fig. 4.3. The parent genomes are separated at random positions and a selection of genes is glued together to form a new genome. This results in a new lattice configuration, the offspring $\mathcal{G}_{\text{off}} = \mathcal{G}_{i \oplus j}$, with properties of both parents. We present a specific example in Fig. 4.3 that contains $N = 5$ molecules, where the offspring inherits the lattice base $\mathbb{V}$ and molecules $(\boldsymbol{R}_1, \boldsymbol{P}_1)$ and $(\boldsymbol{R}_2, \boldsymbol{P}_2)$ from parent one, while its other three molecules stem from parent two.

3. *Random mutation*
   The offspring $\mathcal{G}_{\text{off}}$ is subjected to random mutation moves, with preset probabilities and within suitable numerical boundaries. The goal is to reach disconnected regions of phase space and, thereby, prevent premature convergence to local extrema. These moves include translation

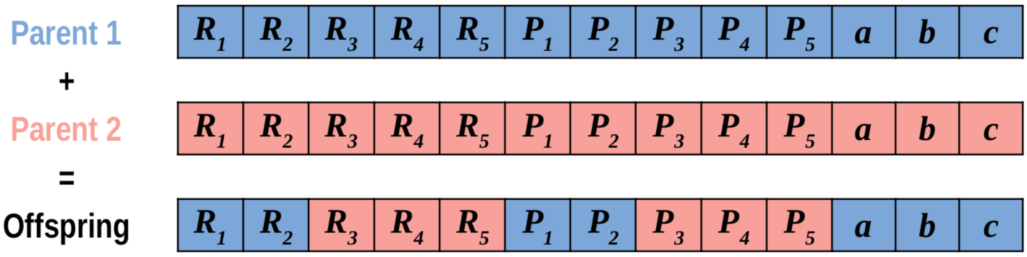

FIG. 4.3.: Visual representation of the genomes of individuals involved in a crossover move. The unit-cell contains $N = 5$ molecules, with positions $\boldsymbol{R}_j$, orientations $\boldsymbol{P}_j$ and lattice base $\mathbb{V} = (\boldsymbol{a}, \boldsymbol{b}, \boldsymbol{c})$.

and rotation of single molecules, changes to the lattice base $\mathbb{V}$ and also swapping of pairs of molecules. The number of molecules N, the unit-cell volume V and thus the packing fraction η_0 (see Table 3.1) are kept constant. Additional types of moves may be included, as long as their effects and potentially emerging biases are taken into account.

II. **Evaluate offspring**

In this next step we decide if the newly created and/or optimized offspring $\mathcal{G}_{\text{off}}$ is a suitable candidate for entering the population $\mathcal{G}^{N_p}$. In principle, the goal is to accept those offspring with the lowest internal energy U, however, the population has to be diverse enough to avoid getting stuck in local minima. Thus, two independent features are taken into account: fitness and so-called ‘nichening’; both of these are introduced below.

1. *Local optimization*

   Each new or changed configuration is subjected to local optimization of the internal energy U via the gradient-descent algorithm L-BFGS-B included in the python *scipy* package. The algorithm iteratively moves from the candidate solution along a gradient to neighboring solutions until either a local convergence is reached or a given number of maximum steps is exhausted. In order to increase the convergence rate of the local optimization we additionally perform ‘basin-dropping’ (BD) steps, i. e. small random moves that are only accepted if they lead to a lower internal energy U. The sequence of alternating L-BFGS-B and BD optimization is performed multiple times to further improve the convergence rate [23].

2. *Check fitness*

   To quantify the fitness, i. e. the quality of individuals, we define the

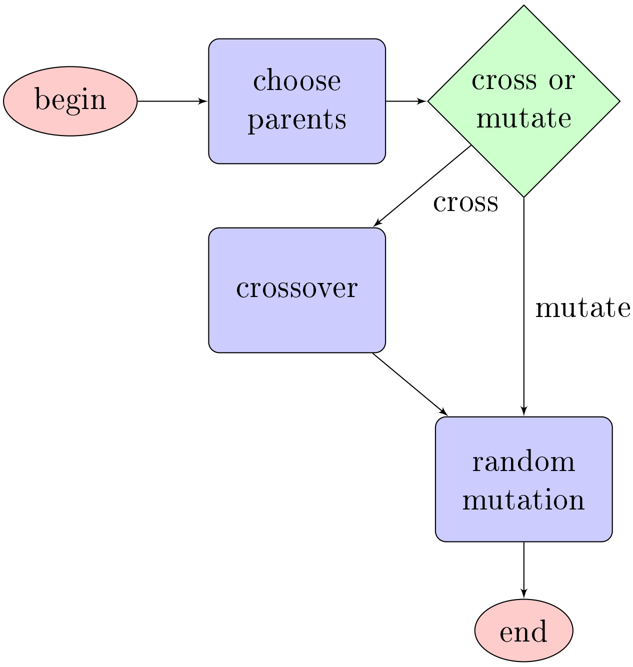

FIG. 4.4.: This flowchart depicts the subprocess of offspring creation. Either two parents are chosen and their properties combined via a crossover move or, alternatively, a single individual is selected. Subsequently, random mutation moves are performed in order to possibly improve the internal energy U.

fitness function [19, 20]

$$F(U) = \exp\left(-s\frac{U - U_{\min}}{U_{\max} - U_{\min}}\right), \tag{4.1}$$

where $U_{\min}$ and $U_{\max}$ are the minimum and maximum internal energies of the current population. $F(U)$ is a monotonic function defined on the interval $0 \leq F(U) \leq F(U_{\min})$. s is the so-called selection parameter that influences the reproduction rate of individuals and is usually set to $s = 3$.

3. *Check available niches*
   In order to guarantee genetic diversity of the population $\mathcal{G}^{N_p}$ the algorithm checks the availability of two kinds of niches, i. e. sufficiently different points in feature space, before accepting a candidate $\mathcal{G}_{\text{off}}$. The first criterion is the availability of a ‘feature-niche’ (or ‘footprint-niche’). Every individual $\mathcal{G}_i$ within the population has a unique feature vector $\boldsymbol{f}_i$ that consists of different order parameters, e. g. the nematic order parameter S (Eq. (2.1)), which are introduced in section 4.2. If the footprint $\boldsymbol{f}_\text{j}$ of the candidate $\mathcal{G}_{\text{off}}$ is too close to any $\boldsymbol{f}_i$ within the population (with respect to the Euclidean distance in feature space $\Delta_{ij} = |\boldsymbol{f}_i - \boldsymbol{f}_j|$), the feature-niche is counted as occupied.

If no feature-niche is available, the difference of the internal energy of $\mathcal{G}_{\text{off}}$ with respect to the internal energy of all current individuals within $\mathcal{G}^{N_p}$ is taken into account. Again, the niche counts as occupied, if the value of $U(\mathcal{G}_{\text{off}})$ is too close to the value of any $U(\mathcal{G}_i)$.

The candidate offspring $\mathcal{G}_{\text{off}}$ is inserted into the population if either a feature-niche is available or, in case of an occupied feature-niche, an energy-niche is identified. Otherwise, $\mathcal{G}_{\text{off}}$ is rejected.

III. **Reject offspring**
If either the fitness of $\mathcal{G}_{\text{off}}$ is too low or the appropriate niches are already occupied within the given parameters, $\mathcal{G}_{\text{off}}$ is rejected and the population $\mathcal{G}^{N_p}$ remains unchanged.

IV. **Update population**
If $\mathcal{G}_{\text{off}}$ results from the random mutation of a single individual and performs better in terms of internal energy, the original lattice configuration is updated.

For a newly created $\mathcal{G}_{\text{off}}$ that is deemed suitable for entering into the population $\mathcal{G}^{N_p}$, the algorithm has to decide which individual has to be replaced. The probability $p(U_i)$ for a non-elite individual $\mathcal{G}_i$ to be replaced depends on the fitness function $F(U_i)$ and the selection parameter s and is given by

$$p(U_i) = \exp\left[-sF(U_i)\right] \left(\sum_{j=1}^{N_p} \exp\left[-sF(U_i)\right] \right)^{-1}, \tag{4.2}$$

which means that individuals with lower fitness are more likely to be replaced.

4.2. Order parameters (OP)

In order to classify all $\mathcal{G}_i$ with respect to their structural properties, we define the feature vector (or footprint vector)

$$\boldsymbol{f}_i = (f_1, .., f_{N_{\text{O}}}), \tag{4.3}$$

where N_{O} is the total number of order parameters (OP) and each f_i represents the evaluation of one OP. To ensure that the Euclidean distance in feature space $\Delta_{ij} = |\boldsymbol{f}_i - \boldsymbol{f}_j|$ represents a meaningful number, each component f_i receives an appropriate weight w_i to account for different parameter ranges and values.

Nematic order parameter S

The nematic order parameter S (see Eq. (2.1)) can assume values between -0.5 and 1; $S = 1$ signifies perfect alignment of all molecules while $S = 0$ indicates isotropy.

Relative director angle ξ

The relative director angle ξ is calculated between the director $\hat{\boldsymbol{n}}$ and the x-axis $\hat{\boldsymbol{x}} = (1, 0, 0)$ and can assume values between 0 and π.

Average distance between COMs

The average distance between the molecule COMs within the unit-cell gives the algorithm the ability to distinguish between different particle arrangements, i. e. to classify how evenly the particles are distributed within the unit-cell.

Total lattice base tilts

This parameter is an indicator for the degree of deformation of the lattice base $\mathbb{V} = (\boldsymbol{a}, \boldsymbol{b}, \boldsymbol{c})$ in comparison to a cuboid unit-cell; this is given by

$$t = b_x + c_x + c_y. \tag{4.4}$$

Orientational order parameter β

The value of β is an alternative indicator for orientational order, calculated by considering the orientations $\hat{\boldsymbol{\omega}}_i$ of nearest neighbors that are identified via Voronoi construction; it is given by

$$\beta = \frac{1}{N} \sum_{i=1}^{N} \frac{1}{\sum_{j \in \mathcal{N}_i} l_{ij}} \sum_{j \in \mathcal{N}_i} l_{ij} |\hat{\boldsymbol{\omega}}_i \cdot \hat{\boldsymbol{\omega}}_j|, \tag{4.5}$$

where N is the number of molecules in the unit-cell, $\mathcal{N}_i$ is the number of Voronoi nearest neighbors of molecule i and l_{ij} is the Voronoi polyhedron surface area separating neighbors i and j [19].

The Voronoi 3D algorithm is implemented in *scipy*. In principle, a polyhedron is constructed around each particle position within the unit-cell, such that all positions within the polyhedron are closer to that particle position than to any other particle center on the lattice, i. e. the periodic continuation of the unit-cell. The polyhedra are space-filling; nearest neighbors share one polyhedron surface [19].

Positional and orientational order parameter α

The combination of positional and orientational order can be quantified via

$$\alpha = \frac{1}{2N} \sum_{i=1}^{N} \frac{1}{\sum_{j\in\mathcal{N}_i} l_{ij}} \sum_{j\in\mathcal{N}_i} l_{ij} |(\hat{\boldsymbol{\omega}}_i \cdot \hat{\boldsymbol{r}}_{ij})^2 + (\hat{\boldsymbol{\omega}}_j \cdot \hat{\boldsymbol{r}}_{ij})^2|, \tag{4.6}$$

where $\hat{\boldsymbol{r}}_{ij}$ is the unit vector between the COMs of molecules i and j, with their respective unit orientations $\hat{\boldsymbol{\omega}}_i$ and $\hat{\boldsymbol{\omega}}_j$. α is also included in the Atuin package [19].

4.3. Implementation

Within this thesis we contributed to the Python 3 framework ‘A totally useful wrapper in evolutionary numerics’ (Atuin) of Ref. [17]; this work implements an MA as introduced in section 4.1 and provides interfaces to the ‘Large-scale Atomic/Molecular Massively Parallel Simulator’ (LAMMPS) [24] for energy calculations of soft matter systems or solid-state materials utilizing various customizable potentials.

4.3.1. Memetic Algorithm Framework: Atuin

The Atuin framework implements an algorithm as described in section 4.1, offers modular building blocks (e. g. GB ellipsoids, LJ spheres, point charges) and wraps the communication with LAMMPS.

The execution of the MA for one specific initial configuration is called a ‘run’. The results are stored as generations of pools that can be evaluated individually. Runs can be continuations of any previous results, i. e. we are able to resume the calculation for any population; with or without changes to the model or system parameters. Thus, we are able to investigate the effect of parameter variation on, for instance, specific equilibrium states. The model parameters are introduced in Table 3.1; the system parameters include the probabilities for specific types of random moves, the number of parallel processes, algorithm specific parameters, LAMMPS settings and more [17, 25].

All model and system parameters, i. e. molecule models, LAMMPS specifics and MA parameters, are defined in YAML (‘YAML Ain’t Markup Language’) format. This makes all configurations highly modular and reusable [26].

Extra features

In order to overcome particular challenges related to the model and the optimization task at hand, we implement the following features:

I. **Ramp compression**

To better be able to handle overlaps caused by the asphericity of the ellipsoids, we perform so-called ramp compression moves with a certain probability when combining the genomes of two individuals via a crossover move. These moves help us to prevent significant molecule overlap that the LG would not, or only with great numerical effort, be able to resolve.

The ramp compression works as follows:

Before placing the molecules on the lattice, the unit-cell volume is inflated by a given value, reducing the packing fraction to η_0^*, so that most potential overlaps are avoided. Subsequently, the unit-cell volume is reduced incrementally until the original packing fraction η_0 is restored. After every volume reduction the system is relaxed via a few restricted LG steps utilizing the *scipy* gradient-descent algorithm L-BFGS-B. The optimization steps are restricted, so that the side-length ratio and tilts of the lattice vectors $\mathbb{V}$ remain unchanged and no molecule swaps occur.

With this method the rejection rate of crossover offspring due to overlaps is reduced significantly (see Fig. 4.5 for a comparison). Fig. 4.5(b) illustrates why the LG cannot resolve the overlap, as the red ellipsoid is completely stuck in its position.

II. **Pool injection**

To test elite individuals of various runs against other populations we employ pool injection, i. e. at the start of a run one or more individuals from one or multiple pools are injected into the current population. This is especially useful to consolidate interim results from independent runs or to introduce a certain bias into a population.

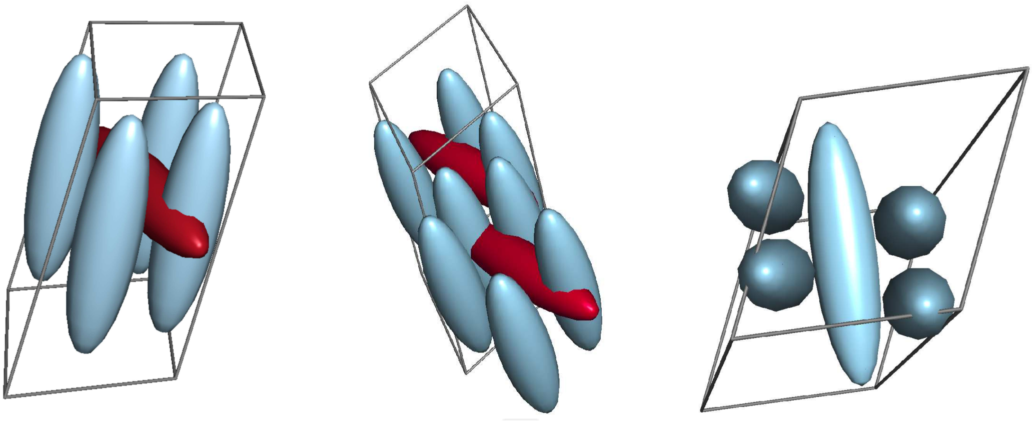

(a) crossover (b) periodic continuation (c) ramped

FIG. 4.5.: Panel (a) shows offspring $\mathcal{G}_{\text{cross}}$ where the red ellipsoid was added in and overlaps significantly. The periodic continuation of $\mathcal{G}_{\text{cross}}$ in panel (b) illustrates why the LG is not able to resolve this situation, as the red ellipsoid is completely stuck in its position. Panel (c) depicts an offspring $\mathcal{G}_{\text{ramp}}$ with the same original genetic makeup after undergoing a ramp compression relaxation.

III. **Orientation snap moves**
In addition to the standard BD moves (positional, orientational, lattice vectors and swaps) we introduce 'orientation snap moves', which with a certain probability change the orientation of single molecules to align them either in parallel or perpendicularly with respect to the director $\hat{\boldsymbol{n}}$. Snap moves introduce a strong bias into the population and the emergence of smectic phases is greatly accelerated; thus, their application should be limited.

4.3.2. Energy Kernel: LAMMPS

The 'Large-scale Atomic/Molecular Massively Parallel Simulator' (LAMMPS) is an open source software package for efficient, parallel, classical molecular dynamics (MD) simulation published under the GNU Public License [24, 25].

In this work we use LAMMPS only as an energy kernel, i. e. every calculation of the total pair potential $U(\boldsymbol{r_{12}}, \boldsymbol{\omega_1}, \boldsymbol{\omega_2})$ is performed in LAMMPS, and do not employ its MD capabilities. All energy contributions to the total pair potential are evaluated via direct lattice summation techniques; the interactions are cut off at certain predefined distances, which guarantee a preset numerical accuracy.

LAMMPS also calculates the forces and torques on the molecule COMs. From these data points Atuin computes the gradient for local optimization.

5. Results

In this chapter we present and classify the meaningful results of the calculations that were performed using the algorithm described in chapter 4. We apply these memetic search strategies to different parameter configurations to investigate the behavior of ILC systems based on the model introduced in chapter 3 at zero temperature. We calculate the energy and properties of resulting lattice configurations to better understand the effect of various model parameters. The calculations are classified into two categories: Biased evolution (BE) of predefined configurations and free evolution (FE).

In this thesis - unless explicitly stated otherwise - all distances are given in units of the ellipsoid diameter $R = 1$ and all energies in terms of the energy scale of the GB pair interaction $\epsilon_0 = 1$, with ratio $\gamma/(R\epsilon_0) = 0.045$ for all calculations, where $\gamma = q^2/(4\pi\varepsilon)$ characterizes the electrostatic energy scale with permittivity ε. From this we define $q_0 = \sqrt{4\pi\varepsilon\gamma}$ as the unit charge.

We employ the python *scikit-learn* implementation [27] of a DBSCAN (Density-Based Spatial Clustering of Applications with Noise) algorithm [28] to identify clusters of molecule COMs via unsupervised learning. This algorithm identifies those points within a set that are closely packed with respect to two parameters: ε-neighborhood and minimum number of points that constitute a cluster. If an arbitrary point in the set has a minimum number of neighbors within a distance ε, a so-called cluster emerges. For any point that is found to be part of the cluster, the algorithm iteratively adds all points from the set that are within its ε-neighborhood. By varying ε we identify layers and columns of the molecule COMs and, subsequently, calculate the normal distances between the clusters: layer spacing d_l and column spacing d_c. Additionally, we introduce the nearest neighbor COM distance $\overline{d}_{cc}$ within the clusters to measure how close to each other the molecule COMs are aligned.

We introduce the following notation for 'individuals' or 'lattice configurations' resulting from FE and BE, respectively:

$$\begin{aligned} \textbf{BE}: \quad & \mathcal{G}_B(N=i,\ \text{label}=\text{b}) && = \mathcal{G}^{\text{b}}_{B(i)}, \\ \textbf{FE}: \quad & \mathcal{G}_F(N=i,\ D=j,\ q=k) && = \mathcal{G}^{j|k}_{F(i)}, \end{aligned}$$

where the label in BE individuals corresponds to specific phases that are approximated, e. g. ‘A’ for the smectic A phase.

5.1. Results obtained from biased evolution (BE)

To perform a biased evolution (BE) search we include well defined lattice configurations $\mathcal{G}^{\mathrm{b}}_{B(N)}$ in the initial populations. In this context, N is the number of molecules in the unit-cell and b is a label, e. g. ‘A’ for smectic A (SmA). With respect to the wide smectic phases (SmAW) reported in Ref. [3], the bias individuals are variations of SmA and SmAW phases.

5.1.1. Bias individuals

The initial BE individuals are prepared for particle numbers of $N \in \{5,\ 10\}$, packing fraction $\eta_0 = 0.325$, charge position $D = \pm 1.8\ R$, charge $q = 1$ and screening length $\lambda^{(q=1)}_{\mathrm{db}} = 5\ R$. The resulting lattice configurations can easily be injected into any populations with the same number of particles in the unit-cell. In Fig. 5.1 and Fig. 5.2 we show the predefined individuals that are introduced in Table 5.1.

Label	Description	Figure
$\mathcal{G}^{\mathrm{A}}_{\mathrm{B}(5)}$	Five densely packed molecules, aligned in parallel, side-by-side in a narrow unit-cell.	Fig. 5.1(a)
$\mathcal{G}^{\mathrm{AW}}_{\mathrm{B}(5)}$	Four densely packed molecules, aligned in parallel, side-by-side in a narrow unit-cell; with a fifth molecule perpendicular.	Fig. 5.1(b)
$\mathcal{G}^{\mathrm{A}}_{\mathrm{B}(10)}$	Ten densely packed molecules, aligned in parallel, in two rows of five in a narrow unit-cell.	Fig. 5.2(a)
$\mathcal{G}^{\mathrm{xAW}}_{\mathrm{B}(10)}$	Seven to nine densely packed molecules, aligned in parallel; with $x = 1$ to $x = 3$ molecules perpendicular.	Fig. 5.2(b)

Tab. 5.1.: Predefined lattice configurations for biased evolution. Fig. 5.1 and Fig. 5.2 show the unit-cells of these individuals.

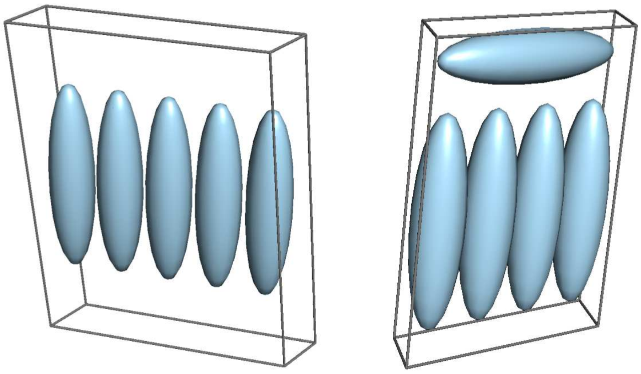
(a) SmA (b) SmAW

FIG. 5.1.: Bias individuals for unit-cells of $N = 5$ particles with packing fraction $\eta_0 = 0.325$, charge $q = 1$, $\lambda_{\text{db}}^{(q=1)} = 5\ R$ and charge position $D = \pm 1.8\ R$. Panel (a) shows a smectic A phase, while panel (b) is a representation of the wide smectic phase AW presented in Ref. [3].

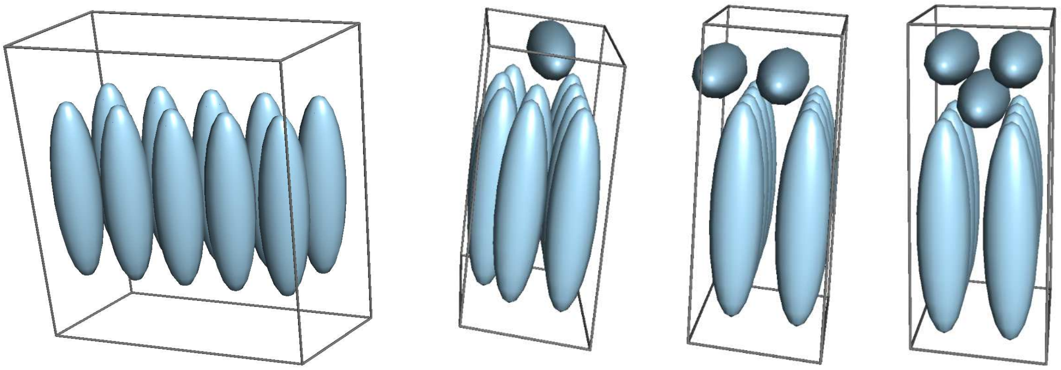
(a) SmA. (b) Variations of SmAW.

FIG. 5.2.: Bias individuals for unit-cells of $N = 10$ particles with packing fraction $\eta_0 = 0.325$, charge $q = 1$, $\lambda_{\text{db}}^{(q=1)} = 5\ R$ and charge position $D = \pm 1.8\ R$. Panel (a) shows a smectic A phase, while panels (b) display representations of the wide smectic phase AW presented in Ref. [3].

5.1.2. Results

The best lattice configurations resulting from simulation runs of BE individuals have two characteristic features in common:

- Lattice configurations based on an SmA phase do not show much change, i. e. the resulting individuals are very similar to the original individuals;
- SmAW individuals transform into SmA-like configurations.

Taking the emerging energies per particle U/N (Fig. 5.3) and the corresponding layer spacing d_l (Fig. 5.4) into account, we find that all SmAW-like lattice configurations eventually reach an SmA-like state. Thus, we conclude that SmAW lattice configurations do not constitute global minima within the observed regions in parameter space. Fig. 5.5 shows the converged results for the lattice configurations $\mathcal{G}^{\mathrm{AW}}_{\mathrm{B}(5)}$ and $\mathcal{G}^{1\mathrm{AW}}_{\mathrm{B}(10)}$, respectively; all individuals listed in Table 5.1 eventually converge towards very similar configurations. For an extended view of such configurations see Fig. 5.6.

We repeated these calculations for various combinations of charge, charge position, packing fraction and GB parameters, but were not able to identify a region in parameter space with a different outcome regarding the dominance of SmA-like lattice configurations over SmAW lattice configurations.

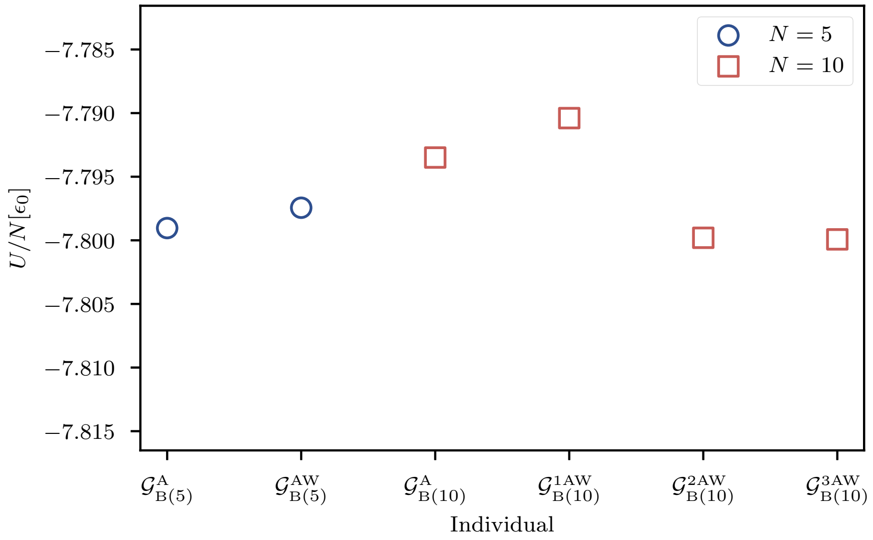

FIG. 5.3.: The energy per particle U/N of the best configurations resulting from the individuals presented in Table 5.1. These calculations where performed for $N \in \{5,\ 10\}$ particles in the unit-cell with a packing fraction of $\eta_0 = 0.325$, charge $q = 1$, charge position $D = \pm 1.8\ R$, GB side-by-side well depth $\epsilon_R = 3$ and screening length $\lambda^{(q=1)}_{\mathrm{db}} = 5\ R$.

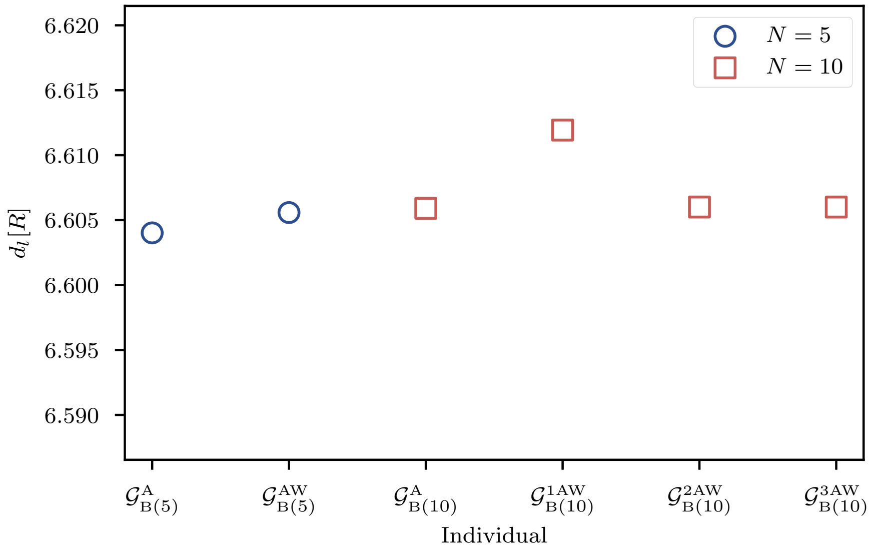

FIG. 5.4.: The layer spacing d_l of the best configurations resulting from the individuals presented in Table 5.1. These calculations where performed for $N \in \{5,\ 10\}$ particles in the unit-cell with a packing fraction of $\eta_0 = 0.325$, charge $q = 1$, charge position $D = \pm 1.8\ R$, GB side-by-side well depth $\epsilon_R = 3$ and screening length $\lambda^{(q=1)}_{\mathrm{db}} = 5\ R$.

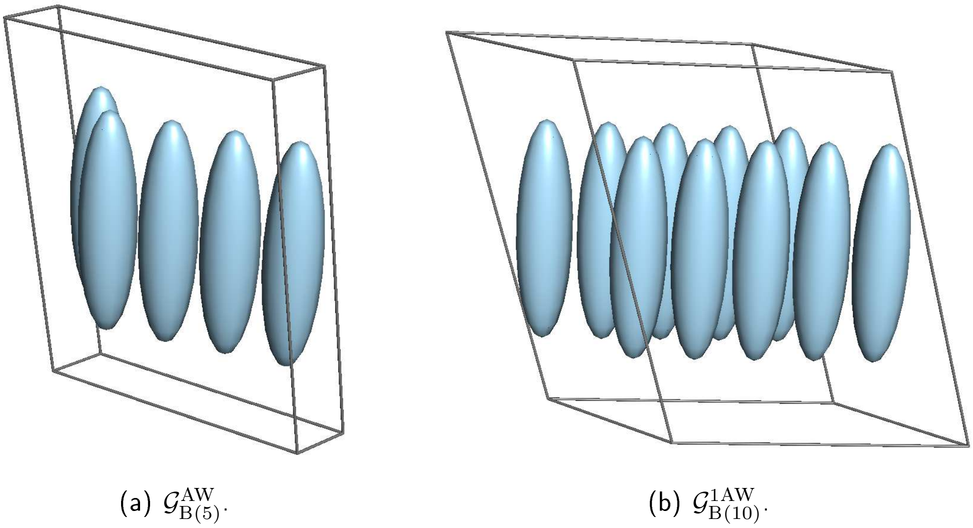
(a) $\mathcal{G}^{\mathrm{AW}}_{\mathrm{B}(5)}$.

(b) $\mathcal{G}^{\mathrm{1AW}}_{\mathrm{B}(10)}$.

FIG. 5.5.: All bias individuals introduced in Table 5.1 converge to slight variations of these unit-cells. Panels (a) and (b) show the results of lattice configurations $\mathcal{G}^{\mathrm{AW}}_{\mathrm{B}(5)}$ and $\mathcal{G}^{\mathrm{1AW}}_{\mathrm{B}(10)}$, respectively.

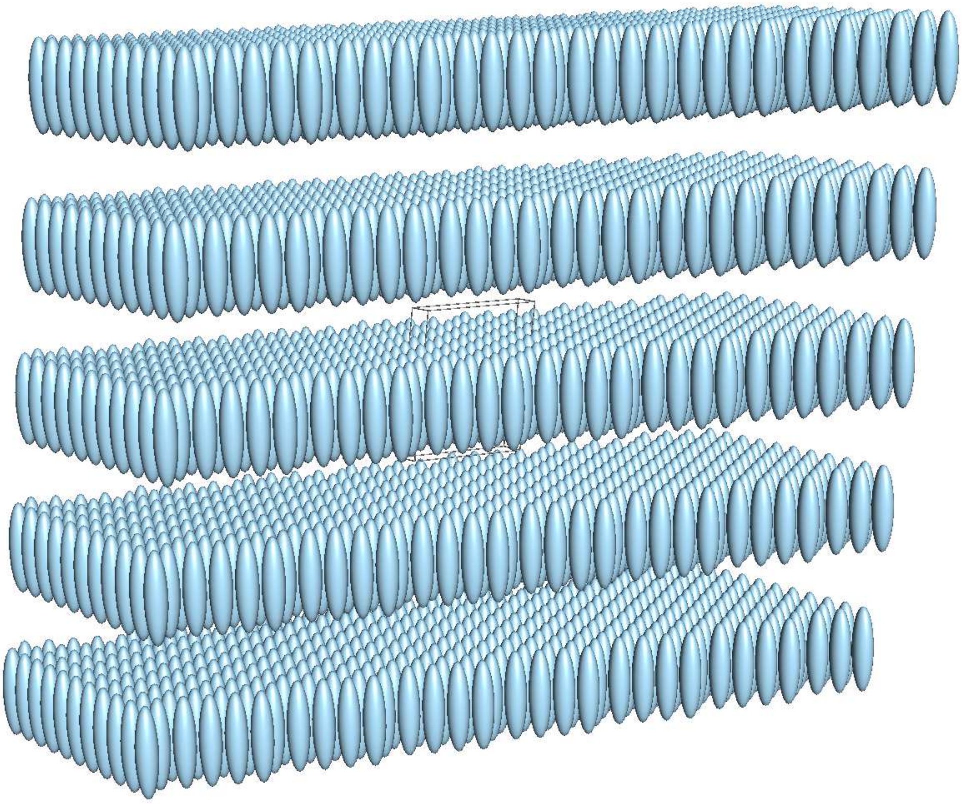

FIG. 5.6.: Extended view of lattice configuration $\mathcal{G}^{\mathrm{A}}_{\mathrm{B}(5)}$ (with layer spacing d_l), which is representative for all converged results of lattice configurations introduced in Table 5.1.

5.2. Results obtained from free evolution (FE)

For a free evolution (FE) search all individuals in the initial population are randomized within given parameter limits. As listed in Table 3.2, we fix the aspect ratio $\kappa = L/R = 4$, the charge count $N_q = 2$, the end-to-end well depth $\epsilon_L = 1$, the GB exponents $\mu = 2$ and $\nu = 1$.

We employ an FE search on systems with unit-cells of $N \in \{5,\ 7,\ 10,\ 12\}$ particles; the majority of calculations is performed for $N = 5$ molecules, as such configurations are computationally less expensive and numerically more stable and thus allow us to investigate more regions within parameter space.

5.2.1. General results

With respect to preliminary calculations performed for various parameter configurations, we focus on $N = 5$ particles in the unit-cell, a packing fraction $\eta_0 = 0.325$ and GB side-by-side well depth $\epsilon_R = 3$; we vary the charge q and the charge position D as listed in Table 5.2. Whenever the charge deviates from $q = 1$, the screening length has to be adjusted from its initial value of $\lambda_{\mathrm{db}} = 5\ R$ via Eq. (3.7); for example $q = 2$ yields $\lambda_{\mathrm{db}}^{(q=2)} = 2.5\ R$.

Parameter	Values
q	$\{0,\ 1,\ 2,\ 3,\ 4\}$
D	$\{0.0\ R,\ \pm 0.9\ R,\ \pm 1.8\ R\}$

Tab. 5.2.: The parameter ranges initially applied in an FE search.

For simplicity, we call charge position $D = 0.0\ R$ ‘center’, $D = \pm 0.9\ R$ ‘intermediate’ and $D = \pm 1.8\ R$ ‘tips’.

Fig. 5.7 shows the total pair potential U/N for different charges and charge positions. In principle, higher charges lead to higher energies as expected, because all charges are positive and thus their interactions increase the energy within the system. This does not seem to hold for individuals with intermediate charge positioning and $q \geq 2$, since $\mathcal{G}_{F(5)}^{0.9|4}$ (violet pentagon) carries the highest charge, but has the lowest energy of these three. These individuals are very similar to each other with respect to energy per particle and unit-cell structure, thus we infer that one or more individuals might be stuck in local energy minima.

To possibly enable the algorithm to leave these presumed local minima, we introduce more variety into the populations by injecting (see section 4.3.1) the best individual of each configuration

$$\mathcal{G}_{F(5)}^{D|q} \quad \text{with } D \in \{0.0\ R,\ \pm 0.9\ R,\ \pm 1.8\ R\}, \quad q \in \{0,\ 1,\ 2,\ 3,\ 4\},$$

and, additionally, the converged result of the bias individual $\mathcal{G}_{\mathrm{B}(5)}^{\mathrm{A}}$, into all of these populations. Giving the systems time to relax and to further evolve, we find the results displayed in Fig. 5.8. Here, the energy per particle U/N increases with the charge q for all charge positions; the enlarged views better illustrate this.

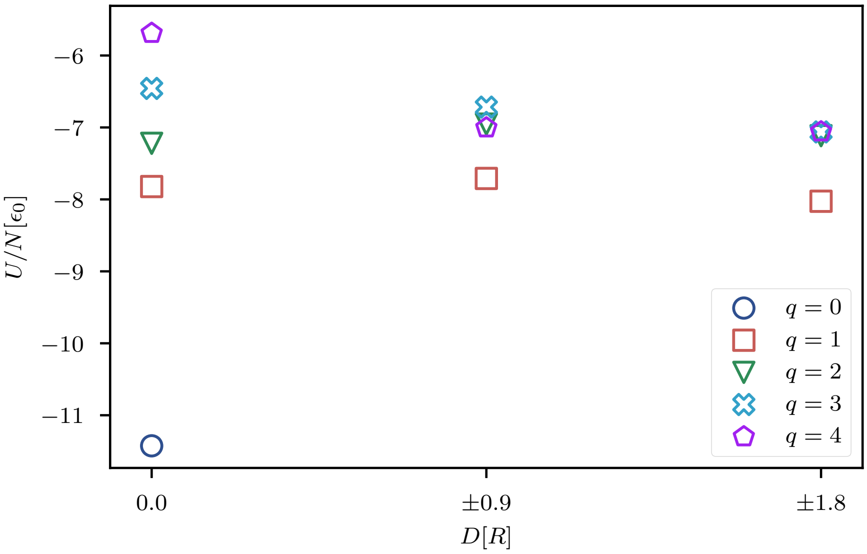

FIG. 5.7.: The energy per particle U/N with respect to the charge position D and the charge q as obtained in an FE search. The corresponding result for uncharged particles (blue circle) is included at charge position $D = 0.0\ R$. These calculations are performed for $N = 5$ particles in the unit-cell with a packing fraction of $\eta_0 = 0.325$.

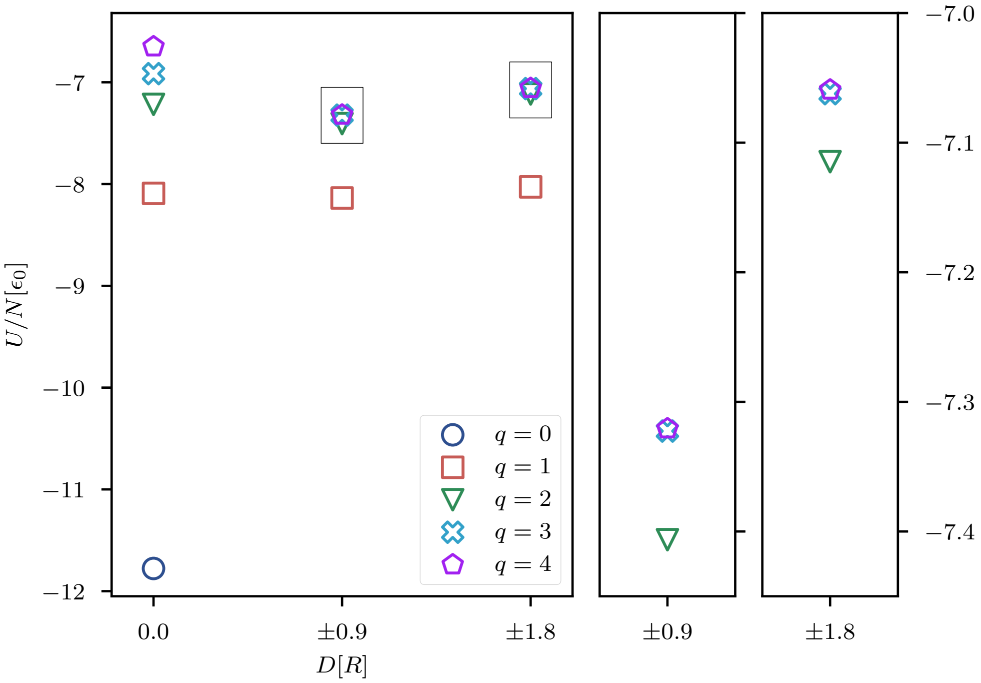

FIG. 5.8.: The main panel shows the energy per particle U/N with respect to the charge position D and the charge q. The corresponding result for uncharged particles (blue circle) is included at charge position $D = 0.0\ R$. These calculations are performed for $N = 5$ particles in the unit-cell with a packing fraction of $\eta_0 = 0.325$. We arrive at these lattice configurations by cross-injecting all results shown in Fig. 5.7 into each population and giving the systems time to relax and to further evolve. The two panels on the right show enlarged views of the results presented in the main panel to better illustrate the data.

Die approbierte gedruckte Originalversion dieser Diplomarbeit ist an der TU Wien Bibliothek verfügbar.
The approved original version of this thesis is available in print at TU Wien Bibliothek.
TU Bibliothek Your knowledge hub WIEN

Summarizing, two distinctively different structures are obtained:

- Dense layers of perfectly aligned molecules ($S > 0.9999$) as shown in Fig. 5.9 and Fig. 5.10, characterized by layer spacing d_l;
- columns of layers of perfectly aligned molecules ($S > 0.9999$) as presented in Fig. 5.11 and Fig. 5.12. The columnar spacing d_c characterizes these lattice configurations in combination with the layer spacing d_l within the columns (see Fig. 5.13).

Both structures show hexagonal alignment of the particle COMs within the layers (as highlighted by orange and blue hexagons drawn onto the layers in Fig. 5.9 and Fig. 5.12).

As already mentioned in the introduction to this chapter, we apply the python *scikit-learn* implementation of the DBSCAN algorithm to group the COMs of particles into connected clusters [27, 28]. We then use these clusters to identify layers and columns and to quantify this classification via layer spacing d_l and column spacing d_c. Fig. 5.10(b), Fig. 5.11(b) and Fig. 5.13 show such clustered COMs.

We calculate the cluster spacing as the minimum distance between all cluster centers $\boldsymbol{c}_i$ projected on the surface normal $\hat{\boldsymbol{s}}_i$ via

$$d_{\min} = \min_{i \neq j}(||(\boldsymbol{c}_i - \boldsymbol{c}_j) \cdot \hat{\boldsymbol{s}}_i||). \tag{5.1}$$

We obtain d_l and d_c by applying Eq. (5.1) on all layer-clusters or all column-clusters, respectively.

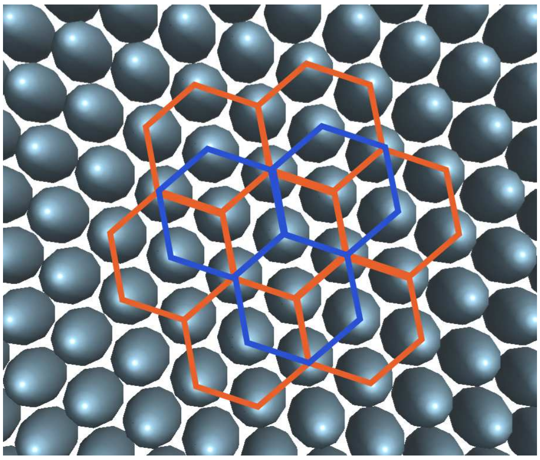

FIG. 5.9.: Top view of one layer of the extended structure presented in Fig. 5.10. The orange and blue lines illustrate the hexagonal alignment of the particles within the layers.

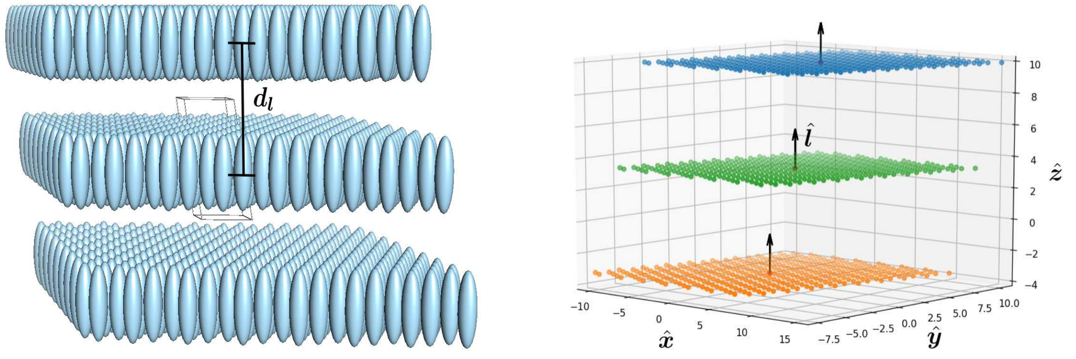
d_l
$\hat{l}$
$\hat{z}$
$\hat{x}$
$\hat{y}$
10
8
6
4
2
0
−2
−4
−10
−5
0
5
10
15
−7.5
−5.0
−2.5
0.0
2.5
5.0
7.5
10.0

(a) Particle layers.

(b) Clustered COMS.

FIG. 5.10.: The left panel shows the periodic continuation of a unit-cell with $N = 5$ particles, packing fraction $\eta_0 = 0.325$, charge $q = 2$ and screening length $\lambda_{\mathrm{db}}^{(q=2)} = 2.5\ R$. d_l denotes the layer distance. In the right panel we see the corresponding particle COMs that are grouped into clusters via the DBSCAN algorithm. The vector $\hat{\boldsymbol{l}}$ is the surface normal of a plane fitted into these COMs. Each color represents one cluster.

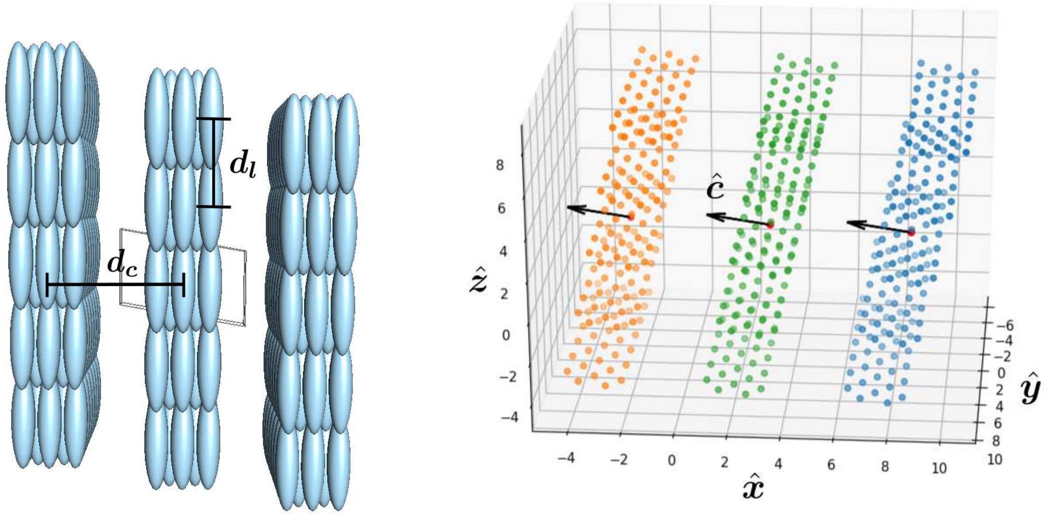
d_l
d_c
$\hat{c}$
$\hat{z}$
$\hat{x}$
$\hat{y}$
8
6
4
2
0
−2
−4
−4
−2
0
2
4
6
8
10
−6
−4
−2
0
2
4
6
8
10

(a) Columns of particle layers.

(b) Clustered COMs.

FIG. 5.11.: The left panel shows the periodic continuation of a unit-cell with $N = 5$ particles, packing fraction $\eta_0 = 0.325$, charge $q = 1$ and screening length $\lambda_{\mathrm{db}}^{(q=1)} = 5\ R$. d_l denotes the layer distance, while d_c is the distance between columns. In the right panel we see the corresponding particle COMs that are grouped into columnar clusters via the DBSCAN algorithm. The vector $\hat{\boldsymbol{c}}$ is the surface normal of a plane fitted into these COMs. Each color represents one cluster.

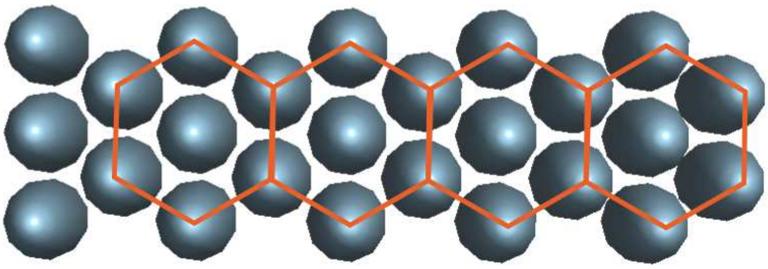

FIG. 5.12.: Top view of one layer within one column of the extended structure presented in Fig. 5.11. The orange lines illustrate the hexagonal alignment of the particles.

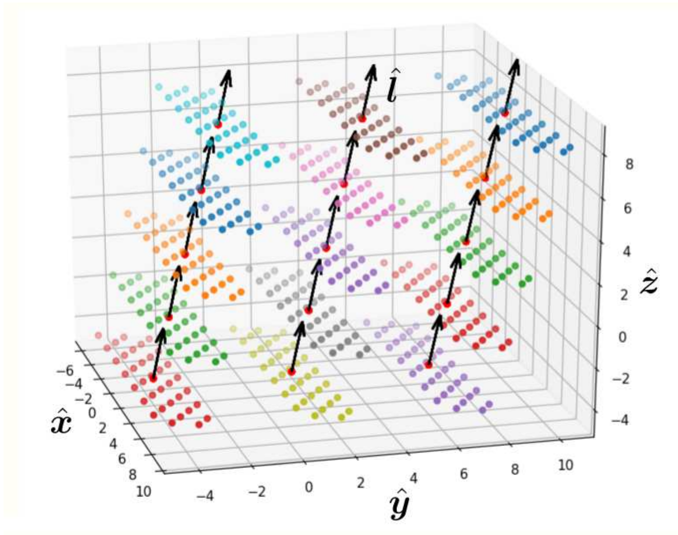

FIG. 5.13.: Layer spacing of the particle COMs within the columns presented in Fig. 5.11(a). The vector $\hat{l}$ is the surface normal of a plane fitted into these COMs. Each color represents one cluster.

Layer spacing d_l

We find that for most parameter combinations the particle layers are grouped into columns and within these columns exhibit small distances between the layers, so that the particle tips of neighboring layers are aligned side-by-side (see Fig. 5.11(a)). The only exceptions in Fig. 5.14 result from the lattice configurations $\mathcal{G}_{F(5)}^{1.8|q}$ (blue triangles) with $q \geq 2$, as for these results no columnar spacing arises and the layer spacing is larger.

Data for d_l are shown in Fig. 5.14. At first glance these results give the impression that for charges $q \geq 2$ the charge value does not influence the layer spacing. This is not entirely true as can be seen from the enlarged views, even though the charge dependency of d_l is rather weak for $q \geq 2$.

We notice the rather abrupt change in layer spacing for $D = \pm 1.8\ R$ from $d_l = 3.17\ R$ (for $q = 1$) to $d_l = 6.60\ R$ (for $q = 2$), this characteristic feature warrants further, detailed investigations. We anticipate that due to the cross-injection already performed between all involved individuals and generous calculation times, these results can be considered as reliable.

In order to better characterize this transition we perform additional FE calculations for charges in the interval $[1,\ 2]$. Fig. 5.15 shows the results of these calculations: As a consequence of the fine resolution in q we can be sure that the transition value of q, q_t can be located in the interval $1.53 < q_t < 1.54$. No lattice configurations with intermediate layer spacing $4.0 \leq d_l \leq 6.0$ have been identified. For $q > q_t$ the energy minimization due to particle arrangement into columns can no longer compensate the Coulomb repulsion between the charges at the particle tips. Thus, individuals with clearly separated, densely packed layers exhibit lower total energies and become dominant. Within the investigated parameter space regions this behavior does not occur for intermediate or center charge positions.

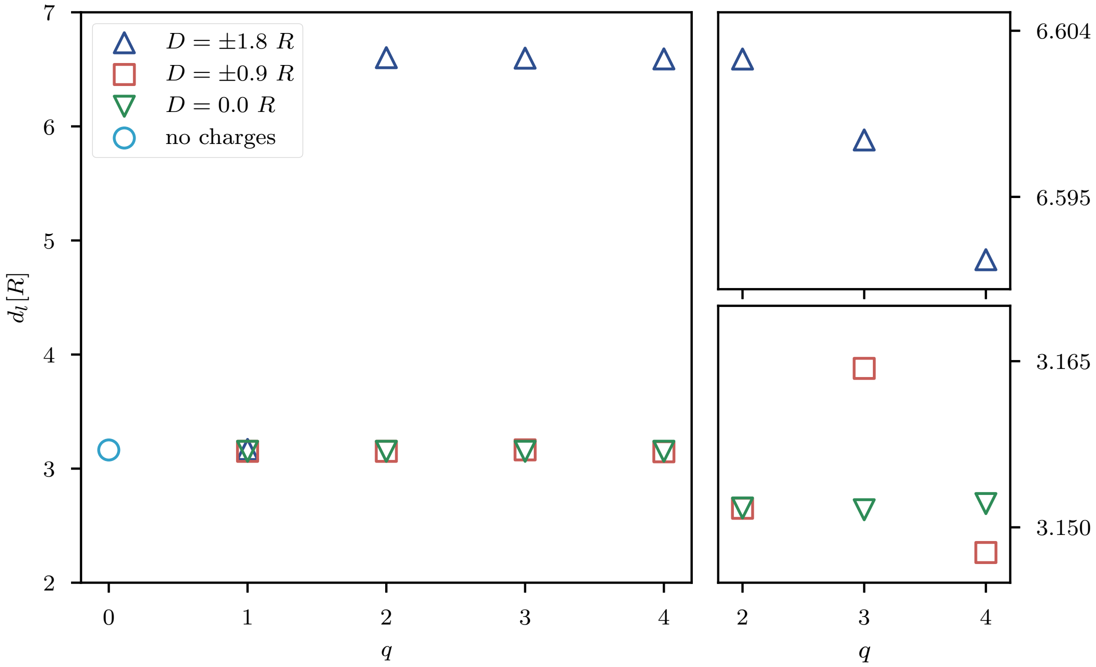

FIG. 5.14.: The left panel shows the layer spacing d_l as obtained for different charges q and charge positions D. To better demonstrate the minute differences in the d_l-values the panels on the side show enlarged views of the data.

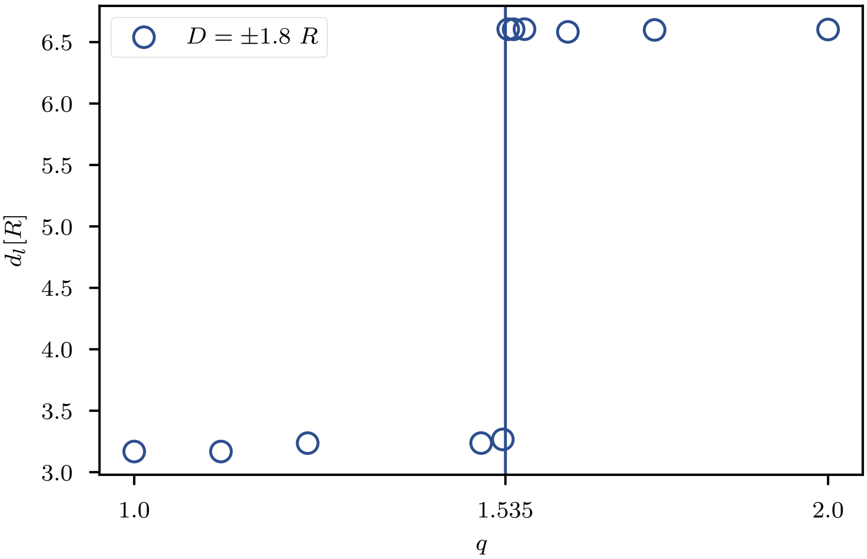

FIG. 5.15.: Enlarged view of the data points shown in Fig. 5.14 for $D = \pm 1.8\ R$ and $q \in [1, 2]$ on a considerably finer grid. The transition value q_t (see text) can be localized to lie in the interval $1.53 < q_t < 1.54$.

Column spacing d_c

All investigated FE configurations with charges at intermediate or center positions converge to lattice configurations that exhibit columnar spacing. Below a threshold of $q \approx 1.54$ this is also true for charges located at the particle tips.

As shown in Fig. 5.16 the columnar spacing is almost constant for center charges (green triangles), while it varies for charges at the intermediate position of $D = \pm 0.9\ R$.

The variations of d_c at $q = 3$ ($\mathcal{G}^{0.9|3}_{\mathrm{F}(5)}$) are consistent with the behavior of the layer spacing d_l in Fig. 5.14 and the average nearest neighbor COM distance $\overline{d}_{\mathrm{cc}}$ (Fig. 5.18), as the lower column spacing coincides with a higher layer spacing and a higher particle density within the layers at a constant volume. In contrast, the particles in $\mathcal{G}^{0.9|4}_{\mathrm{F}(5)}$ are less densely packed, thus the differences in d_l and d_c are less pronounced.

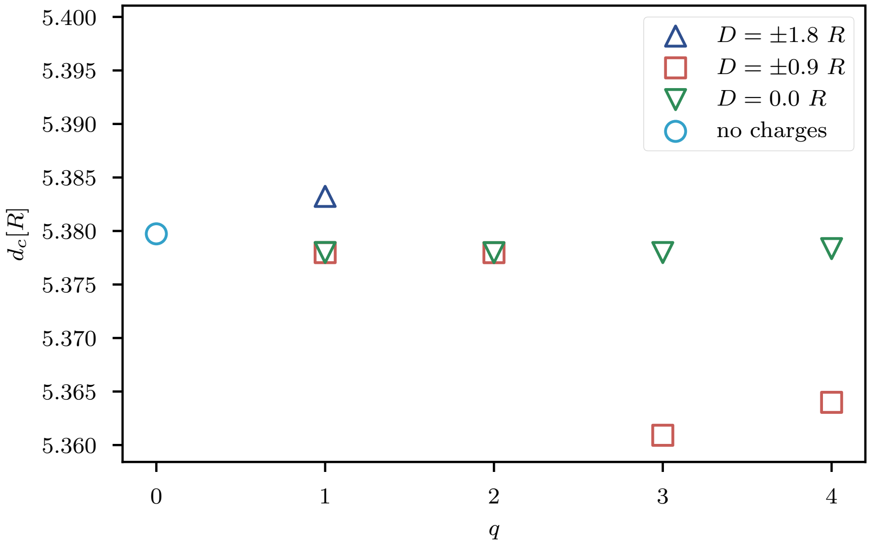

FIG. 5.16.: Column spacing d_c for various values of charge q and charge position D.

Particle density within layers

While the average distance of COMs defined in section 4.2 is well suited as an order parameter to increase diversity and, consequently, the emergence of different particle configurations within the unit-cell, it is not useful for the determination of the particle density within a layer, as it only includes the unit-cell particles and, also, is not limited to nearest neighbors. Fig. 5.17 illustrates this: The average over all COM distances between the particles shown in panel (a), including for example the distances a, b and c between particles, will be significantly larger than the nearest neighbor COM distance d_{cc} in panel (b).

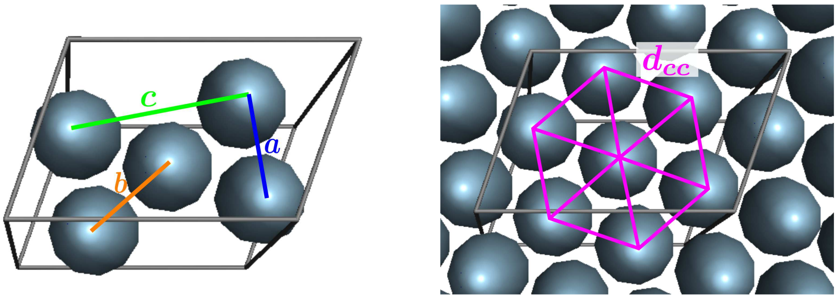

(a) $\mathcal{G}^{0.9|3}_{F(5)}$ unit-cell.   (b) $\mathcal{G}^{0.9|3}_{F(5)}$ periodic continuation.

FIG. 5.17.: Comparison of the COM distances within the unit-cell of $\mathcal{G}^{0.9|3}_{F(5)}$ in panel (a) to the COM distances within the corresponding extended structure in panel(b) to illustrate the impracticality of the average distance within the unit-cell as a measure of COM density within the layer.

Thus, in order to quantify the particle density within a layer, we look at the average distance between COMs of nearest neighbors $\overline{d}_{cc}$.

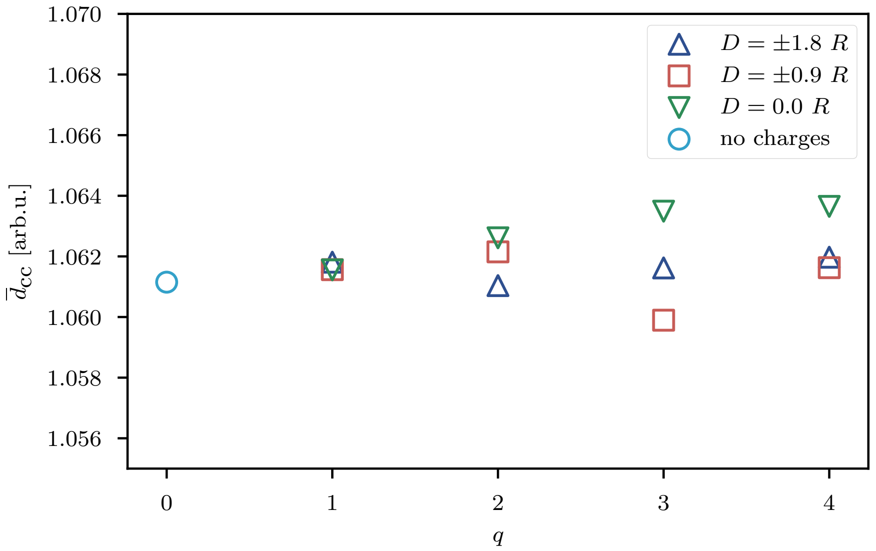

FIG. 5.18.: The average nearest neighbor COM distance $\overline{d}_{\mathrm{cc}}$ within a layer of clustered particles; calculated for an extended structure of 3×3 unit-cells. These calculations where performed for $N = 5$ particles in the unit-cell with a packing fraction of $\eta_0 = 0.325$.

In Fig. 5.18 we notice that for charges located in the center (including charge zero) $\overline{d}_{\mathrm{cc}}$ increases monotonously. For charges located at the particle tips (blue triangles), we observe that the particles are more densely packed when the overall structure switches from columnar for $q = 1$ to pure layers for $q = 2$; then $\overline{d}_{\mathrm{cc}}$ grows again with higher charges. The behavior for intermediate charges (red squares) for $q = 3$ coincides with considerably higher layer spacing d_l (see Fig. 5.14).

5.2.2. Complementary calculations

We have performed calculations for larger numbers of particles in the unit-cell to investigate the influence of various system parameters on our previous observations and to assess the stability and performance of the algorithm.

Impact of the packing fraction on layer spacing

To speed-up the calculation required to obtain additional data points we apply the cross-injection method, i. e. all available lattice configurations resulting from previous FE runs are injected into random populations for packing fractions of $\eta_0 \in \{0.275,\ 0.35,\ 0.375,\ 0.4\}$ and charges $q \in \{1,\ 2\}$. In Fig. 5.19 we then compare these results to data points previously determined via FE search for packing fractions $\eta_0 = 0.3$ and $\eta_0 = 0.325$. We observe that the change from columnar layers to densely packed layers occurs for the majority of the investigated packing fractions. The layer spacing d_l is very similar for all data points for $q = 1$, but inversely proportional to η_0 for $q = 2$. At packing fractions of $\eta_0 \in \{0.275,\ 0.4\}$ the columnar clustering prevails for $q = 2$. We assume that for $\eta_0 = 0.4$ the unit-cell is too small to achieve sufficient layer spacing to suppress columnar alignment, while for $\eta_0 = 0.275$ the column spacing becomes large enough to persist for charge $q = 2$.

Impact of the GB side-by-side well depth ϵ_R

From the data shown in Fig. 3.9 we conclude that our system behaves differently for a GB side-by-side well depth of $\epsilon_R = 1$ as compared to $\epsilon_R = 3$: The side-by-side alignment of ellipsoids is now no longer preferred over an end-to-end alignment, thus the densely packed layers for charges $q \geq 2$ are replaced by columnar clusters. The charges are now more likely to avoid their neighbor's charges which gives rise to zigzag alignment (see Fig. 5.20).

In the previous calculations, the GB potential well depth ratio of $\epsilon_R/\epsilon_L = 3$ led to perfectly aligned ellipsoids in all individuals. For $\epsilon_R/\epsilon_L = 1$ the side-by-side

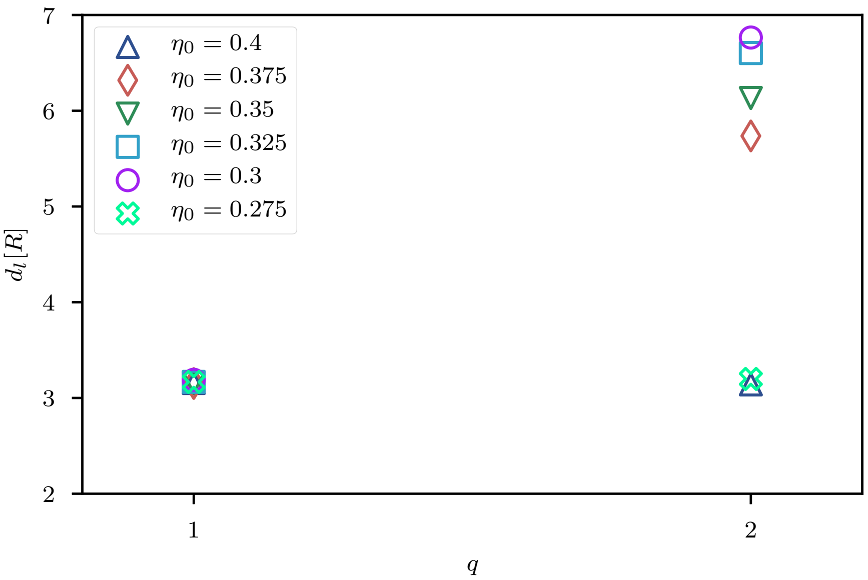

FIG. 5.19.: Comparison of the layer spacing d_l for charges $q \in \{1,\ 2\}$ for various packing fractions.

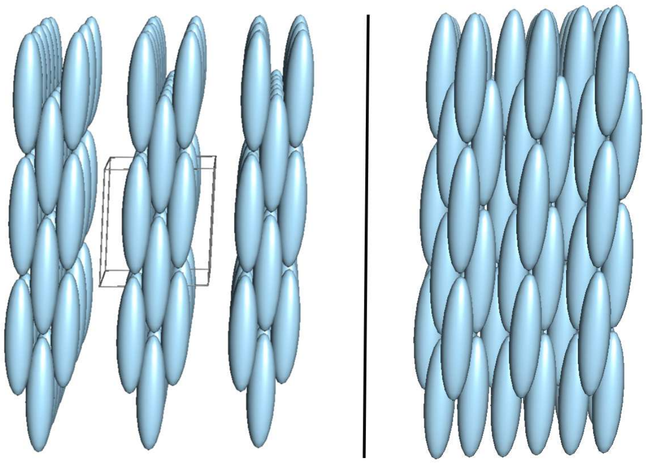

FIG. 5.20.: Two side views of the periodically extended result of $\mathcal{G}^{1.8|2}_{\mathrm{F}(5)}$ with $\epsilon_R = 1$. As the side-by-side alignment is no longer preferred over the end-to-end alignment, the charges are more likely to avoid their neighbors, giving rise to a zigzag alignment.

alignment is no longer dominant and thus the emerging lattice configurations are more diverse and require more computational resources. For that reason, the energy per particle U/N (Fig. 5.21) and column spacing d_c (Fig. 5.22) are not as reliable as in previous results. Noticeably, U/N for center charges is higher for $q = 2$ than for $q = 4$. Furthermore, the column spacing shows different trends for the different charge positions. For center charges d_l is almost constant, while d_l shows a minimum for $q = 2$ for intermediate charge positions and drops monotonously with increasing q for charges at the particle tips.

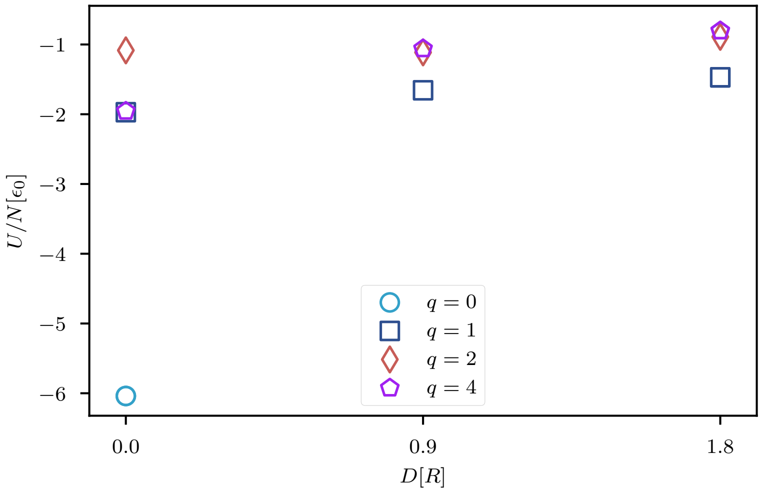

FIG. 5.21.: Energy per particle U/N for different charges and charge positions. The calculations were performed for a packing fraction $\eta_0 = 0.325$ and GB well depth $\epsilon_R = 1$.

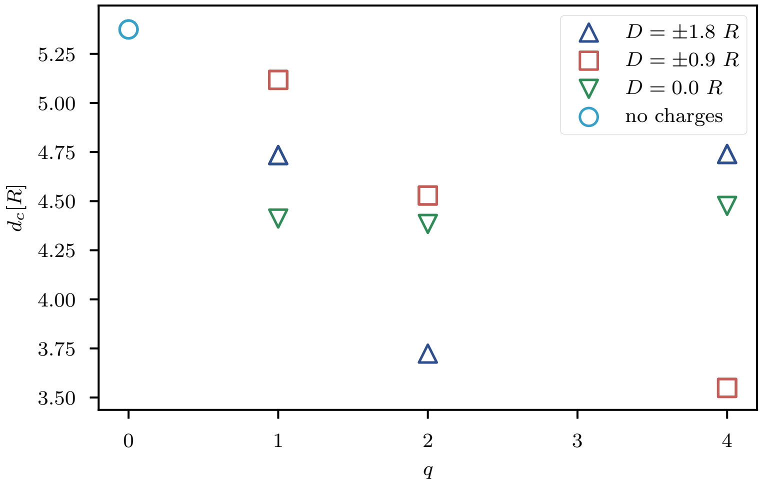

FIG. 5.22.: Column spacing d_c for different charges and charge positions. The calculations were performed for a packing fraction $\eta_0 = 0.325$ and GB well depth $\epsilon_R = 1$.

Impact of different values of N

Fig. 5.23 compares energy per particle U/N, layer spacing d_l and column spacing d_c for $N \in \{5,\ 7,\ 10,\ 12\}$ for charge $q = 0$. All resulting individuals are columnar and U/N and d_l are both rather stable with respect to different N. We notice that d_c increases with N, but that can be attributed to Eq. (5.1), where we calculate the distance between cluster centers. Thus, the larger column spacing stems from wider layers within the columns and not from additional empty space inbetween.

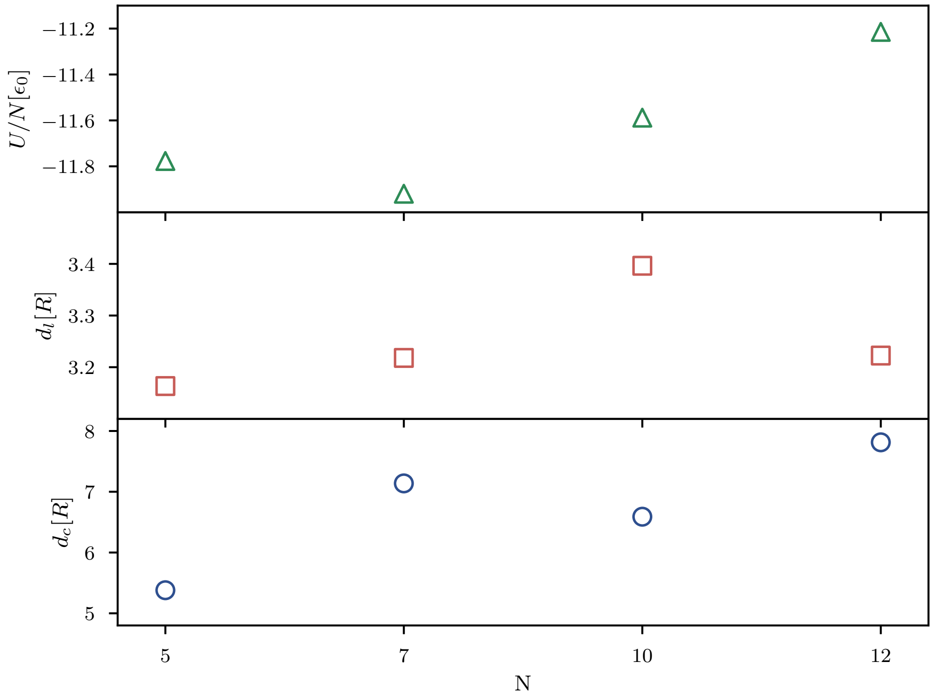

FIG. 5.23.: Comparison of energy per particle U/N (top panel), layer spacing d_l (center panel) and column spacing d_c (bottom panel) for different numbers of particles in the unit-cell, $N \in \{5,\ 7,\ 10,\ 12\}$, and charge $q = 0$.

For $N = 7$ particles in the unit-cell the behavior documented with respect to charge position $D = \pm 1.8\ R$ in Fig. 5.14 still holds; columnar structures emerge for $q = 1$ and densely packed layers form at higher charges (verified for $q = 4$). Furthermore, we observe that the seven particles organize themselves into a hexagonal alignment within the unit-cell (see Fig. 5.24).

For particle numbers $N \geq 10$ the columnar structure prevails for charge $q \geq 2$, located near the particle tips. Fig. 5.25 shows the energy per particle U/N for different charges and charge positions and for five and ten particles in the unit-cell,

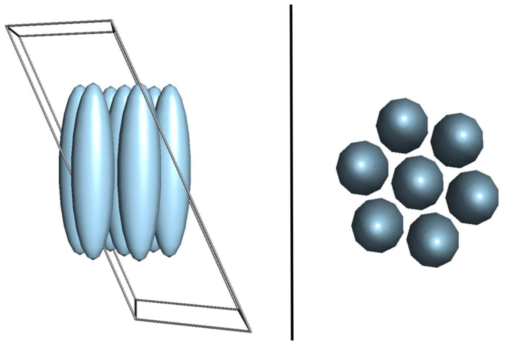

FIG. 5.24.: Hexagonal structure of the particles in the unit-cell of $\mathcal{G}^{1.8|4}_{\mathrm{F}(7)}$.

respectively. We notice that the dependence on the charge positions shows the same trend for either particle number: U/N is lowest for charges at the intermediate position. All energies calculated for $N = 10$ are higher than their $N = 5$ counterparts, thus we conclude that these configurations did not arrive at a global minimum within the given calculation time frame.

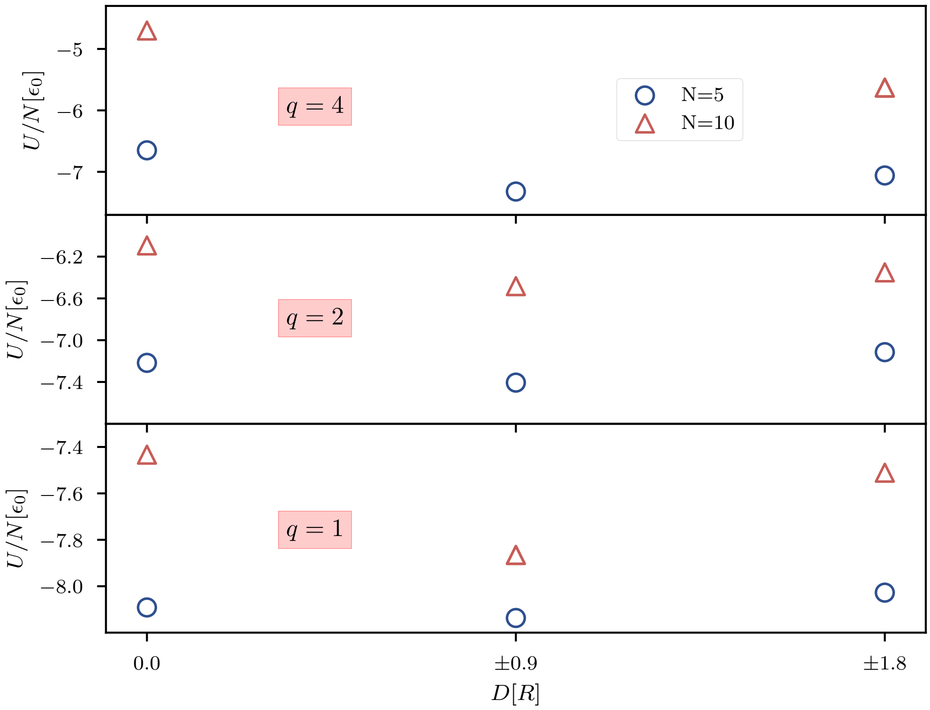

FIG. 5.25.: Comparison of energy per particle U/N for charge $q = 4$ (top panel), $q = 2$ (center panel) and $q = 1$ (bottom panel) with respect to the charge positions; for five (blue circles) and ten (red triangles) particles in the unit-cell, respectively. The data point for $\mathcal{G}^{0.9|4}_{\mathrm{F}(10)}$ is not available.

6. Summary and Conclusion

We studied ordered ground state configurations of systems of ionic liquid crystals (ILCs) at zero temperature and observed the emergence of columnar structures and densely packed layers. These investigations were realized by introducing a suitable model for ILCs and by using a numerical algorithm based on evolutionary search strategies and local optimization, that enabled us to identify such configurations in an efficient and reliable manner; we utilized the 'Large-scale Atomic/Molecular Massively Parallel Simulator' (LAMMPS) as an energy kernel for our calculations.

We introduced a model related to the one used by Bartsch et al. [3] and Kondrat et al. [8] to mimick the characteristic features of ILCs, i. e. shape anisotropy and charges. To this end we combined a Gay-Berne potential with screened Coulomb interactions. We documented the impact of different model and system parameters on the self-assembly scenarios in order to gain a better understanding of the model.

Two simulation methods were employed: Biased evolution (BE) and free evolution (FE). Through BE we observed that at zero temperature wide smectic arrangements as reported by Bartsch et al. [3] consistently performed worse with respect to energy per particle U/N than other structures; this observation makes sense since Bartsch et al. [3] originally obtained their results at finite temperatures. However, we did find configurations with significant spacing between the layers.

The majority of FE simulations were performed for systems consisting of unit-cells of five particles and a packing fraction $\eta_0 = 0.325$. We found that particles that carry charges near their tips changed their spatial arrangement in a discontinuous fashion near a charge threshold of $q \approx 1.535$. Above that transition point we found densely packed layers of perfectly aligned particles, while below that limit the layers were arranged in columnar structures along one direction; both shapes showed hexagonal alignment of the particles within the layers. This transition was verified over a range of packing fractions and also for unit-cells containing seven particles.

We performed additional calculations, extending thereby the investigated parameter space and testing the stability of our algorithm. For unit-cells with ten or more particles the algorithm required a significantly larger amount of computational resources to converge and was more prone to being stuck in local minima, due to the higher complexity of the problem. To counteract this behavior in future applications it might be beneficial to generate ensembles of lattice configurations from different random initial conditions and combine their results through cross-injection or similar methods.

The present model and the applied numerical algorithm might be well suited to investigate systems of polarized ellipsoids as introduced by Azari et al. [29] without too many adjustments. Polarized particles are electrically neutral without the presence of counterions and thus the Coulomb interaction would no longer be screened by a counterion-background and long range interaction would have to be taken into account; this functionality is included in LAMMPS, e. g. via Ewald summation [19, 25, 30, 31].

Future simulations within this context should focus on different particle aspect ratios and, thereby, investigate the role of the degree of shape anisotropy on the ordered ground states. At the same time it would make sense to optimize the algorithm in terms of larger unit-cells. Furthermore, the restriction of only using identical charges and symmetrical charge positioning should be scrutinized, while also including significantly higher charge values. The use of LAMMPS as our energy kernel enables us to systematically extend the model with different types of potentials that are included in the software package.

A. Algorithm Keywords

Configuration
All settings regarding the computation, algorithm and system parameters constitute one specific configuration.

Elite
The best individuals (i. e. those with the lowest energy) are protected against direct (random) replacement. These elite individuals remain in the pool until a certain number of individuals with better energy crowd them out.

Footprint
The footprint of an individual includes the values of all order parameters and, thereby, quantifies an individual.

Generation
The replacement or insertion of one individual and subsequent reordering of the population constitutes a new generation, hence, a generation in this context does not correspond to the usual biological meaning.

Individual
One lattice configuration or genome, i. e. one point in phase space.

Move
Moves happen on different scales that range from changing the position of one particle to mixing two individuals via a crossover. In principle, moves are computational steps that change existing or create new individuals.

Niche
A niche is a fraction of feature space identified by a combination of order parameters. Offspring have a higher chance of being added to the pool if they belong to an unoccupied niche and thus diversify the population.

Offspring
The individuals arising from crossover moves and/or optimization are called offspring. Depending on their energy and what niche they belong in, these offspring are either added to the pool or discarded.

Parent
To create an offspring the properties of two parents are combined.

Pool
The collection (population) of individuals the algorithm produces and/or operates on. The pool is subject to continual change as more suitable individuals replace others.

Run
A run is the execution of the memetic algorithm for one specific initial configuration, that results in generations of pools. Runs can be continuations of previous runs; with or without changes to the configuration.

Worker
Multiple processes work in parallel on creating new offspring or improving existing ones. These processes are called workers.

Bibliography

[1] P. G. de Gennes. *The Physics of Liquid Crystals*. Oxford Science Publications. Clarendon Press, Oxford [u.a.], 2. ed., 1. publ. in paperback. edition, 1995. ISBN 978-0-19-851785-6.

[2] M. Kleman and O. D. Laverntovich. *Soft Matter Physics: An Introduction*. Partially Ordered Systems. Springer-Verlag, New York, 2003. ISBN 978-0-387-95267-3.

[3] H. Bartsch, M. Bier, and S. Dietrich. Smectic phases in ionic liquid crystals. *Journal of Physics: Condensed Matter*, 29(46):464002, October 2017. ISSN 0953-8984. doi: 10.1088/1361-648X/aa9090.

[4] I. Georgiou. *Simulations of Soft Matter Systems*. PhD thesis, Technische Universität Wien, Vienna, 2014.

[5] K. Binnemans. Ionic Liquid Crystals. *Chemical Reviews*, 105(11):4148–4204, November 2005. ISSN 0009-2665, 1520-6890. doi: 10.1021/cr0400919.

[6] K. Goossens, K. Lava, C. W. Bielawski, and K. Binnemans. Ionic Liquid Crystals: Versatile Materials. *Chemical Reviews*, 116(8):4643–4807, April 2016. ISSN 0009-2665. doi: 10.1021/cr400334b.

[7] T. Kato, M. Yoshio, T. Ichikawa, B. Soberats, H. Ohno, and M. Funahashi. Transport of ions and electrons in nanostructured liquid crystals. *Nature Reviews Materials*, 2(4):1–20, March 2017. ISSN 2058-8437. doi: 10.1038/natrevmats.2017.1.

[8] S. Kondrat, M. Bier, and L. Harnau. Phase behavior of ionic liquid crystals. *The Journal of Chemical Physics*, 132(18):184901, May 2010. ISSN 0021-9606. doi: 10.1063/1.3417384.

[9] M. P. Allen and D. J. Tildesley. *Computer Simulation of Liquids: Second Edition*. Oxford University Press, June 2017. ISBN 978-0-19-184143-9.

[10] B. J. Berne and P. Pechukas. Gaussian Model Potentials for Molecular Interactions. *The Journal of Chemical Physics*, 56(8):4213–4216, April 1972. ISSN 0021-9606. doi: 10.1063/1.1677837.

[11] J. G. Gay and B. J. Berne. Modification of the overlap potential to mimic a linear site–site potential. *The Journal of Chemical Physics*, 74(6):3316–3319, March 1981. ISSN 0021-9606. doi: 10.1063/1.441483.

[12] R. Berardi, C. Fava, and C. Zannoni. A generalized Gay-Berne intermolecular potential for biaxial particles. *Chemical Physics Letters*, 236(4):462–468, April 1995. ISSN 0009-2614. doi: 10.1016/0009-2614(95)00212-M.

[13] R. Berardi, C. Fava, and C. Zannoni. A Gay–Berne potential for dissimilar biaxial particles. *Chemical Physics Letters*, 297(1):8–14, November 1998. ISSN 0009-2614. doi: 10.1016/S0009-2614(98)01090-2.

[14] P. Moscato. *On Evolution, Search, Optimization, Genetic Algorithms and Martial Arts - Towards Memetic Algorithms.* 1989.

[15] G. E. P. Box and K. B. Wilson. On the Experimental Attainment of Optimum Conditions. In Samuel Kotz and Norman L. Johnson, editors, *Breakthroughs in Statistics*, pages 270–310. Springer New York, New York, NY, 1992. ISBN 978-0-387-94039-7 978-1-4612-4380-9. doi: 10.1007/978-1-4612-4380-9_23.

[16] R.G. Brereton. Steepest Ascent, Steepest Descent, and Gradient Methods. *Comprehensive Chemometrics*, 1:577–590, January 2010. doi: 10.1016/B978-044452701-1.00037-5.

[17] B. Hartl, S. Sharma, O. Brügner, S. F. L. Mertens, M. Walter, and G. Kahl. Reliable identification of ordered ground state configurations of complex molecules under electrochemical conditions. *submitted to J. Chem. Theory Comput.*, 2019.

[18] K. Deb. An introduction to genetic algorithms. *Sadhana*, 24(4):293–315, August 1999. ISSN 0973-7677. doi: 10.1007/BF02823145.

[19] M. Antlanger. *Ordered Equilibrium Structures in Systems with Long-Range Interactions, Structures Ordonées Dans Les Systèmes à Longue Portée.* PhD thesis, Technische Universität Wien, Vienna, 2015.

[20] G. Doppelbauer. *Ordered Equilibrium Structures of Patchy Particle Systems.* PhD thesis, Technische Universität Wien, Vienna, 2012.

[21] M. Mitchell. *An Introduction to Genetic Algorithms.* MIT Press, Cambridge, MA, USA, 1996. ISBN 978-0-262-13316-6.

[22] D. E. Goldberg. *Genetic Algorithms in Search, Optimization and Machine Learning.* Addison-Wesley Longman Publishing Co., Inc., Boston, MA, USA, 1st edition, 1989. ISBN 978-0-201-15767-3.

[23] E. Jones, T. Oliphant, and P. Peterson. SciPy: Open Source Scientific Tools for Python. 2001.

[24] S. Plimpton. Fast Parallel Algorithms for Short-Range Molecular Dynamics. *Journal of Computational Physics*, 117(1):1–19, March 1995. ISSN 0021-9991. doi: 10.1006/jcph.1995.1039.

[25] LAMMPS Documentation. https://lammps.sandia.gov (accessed 09.12.2019, 13:01:00).

[26] The Official YAML Web Site. https://yaml.org/ (accessed 23.11.2019, 11:31:59).

[27] F. Pedregosa, G. Varoquaux, A. Gramfort, V. Michel, B. Thirion, Olivier Grisel, Mathieu Blondel, Peter Prettenhofer, Ron Weiss, Vincent Dubourg, Jake Vanderplas, Alexandre Passos, David Cournapeau, Matthieu Brucher, Matthieu Perrot, and Édouard Duchesnay. Scikit-learn: Machine Learning in Python. *Journal of Machine Learning Research*, 12:2825–2830, October 2011. ISSN 1533-7928.

[28] P. Liu, D. Zhou, and N. Wu. VDBSCAN: Varied Density Based Spatial Clustering of Applications with Noise. In *2007 International Conference on Service Systems and Service Management*, pages 1–4, June 2007. doi: 10.1109/ICSSSM.2007.4280175.

[29] A. Azari, J. J. Crassous, A. M. Mihut, E. Bialik, P. Schurtenberger, J. Stenhammar, and P. Linse. Directed Self-Assembly of Polarizable Ellipsoids in an External Electric Field. *Langmuir*, 33(48):13834–13840, December 2017. ISSN 0743-7463. doi: 10.1021/acs.langmuir.7b02040.

[30] M. Mazars. Long ranged interactions in computer simulations and for quasi-2D systems. *Physics Reports*, 500(2-3):43–116, 2011. ISSN ISSN 0370-1573. doi: 10.1016/j.physrep.2010.11.004.

[31] P. P. Ewald. Die Berechnung optischer und elektrostatischer Gitterpotentiale. *Annalen der Physik*, 369(3):253–287, 1921. ISSN 1521-3889. doi: 10.1002/andp.19213690304.